

11-19-2014

# Developments of Gigapixel Microscopy

SIYUAN DONG

siyuandong.bme@gmail.com

---

## Recommended Citation

DONG, SIYUAN, "Developments of Gigapixel Microscopy" (2014). *Master's Theses*. 687.  
[https://opencommons.uconn.edu/gs\\_theses/687](https://opencommons.uconn.edu/gs_theses/687)

This work is brought to you for free and open access by the University of Connecticut Graduate School at OpenCommons@UConn. It has been accepted for inclusion in Master's Theses by an authorized administrator of OpenCommons@UConn. For more information, please contact [opencommons@uconn.edu](mailto:opencommons@uconn.edu).

# Developments of Gigapixel Microscopy

Siyuan Dong

B.S., Zhejiang University, 2013

A Thesis

Submitted in Partial Fulfillment of the

Requirements for the Degree of

Master of Engineering

At the

University of Connecticut

2014

Copyright by

Siyuan Dong

[2014]

# APPROVAL PAGE

Masters of Engineering Thesis

## Developments of Gigapixel Microscopy

Presented by

Siyuan Dong, B.S.

Major Advisor \_\_\_\_\_  
Guoan Zheng

Associate Advisor \_\_\_\_\_  
Quing Zhu

Associate Advisor \_\_\_\_\_  
Kazunori Hoshino

University of Connecticut

2014

## **Acknowledgements**

This work would not have been possible without the help of many talented people at University of Connecticut. I want to thank my advisor, Dr. Guoan Zheng for guidance and support. I was totally a greenhorn to optical imaging area when I came to UCONN. I really appreciate the patient directions from Dr. Guoan Zheng and I learn a lot from him. Many thanks to the members of Prof. Zheng' group over the one and a half years, Kaikai Guo, Zichao Bian, Jun Liao, Radhika Shiradkar, Pariksheet Nanda. Working with all of you is one of the best memories in my life. I thank my friend Quichen Dong for his help and encouragements in my daily life. I thank my friends Hasan Fiaz, Jianan Lin, Chenlu Yu, my seniors Zhen Cao, Yang Guo, Xiaoyu Ma, and Jun Chen.

I thank my parents for helping me throughout my study abroad and offering their support whenever needed. To my girlfriend, I am deeply grateful for her patience and encouragement along this journey towards my degree at University of Connecticut.

## Table of contents

Acknowledgements-----	4
Abstract-----	7
List of Figures-----	9
1. Introduction-----	12
1.1 Introduction to Fourier ptychographic microscope-----	12
1.2 The principle of Fourier ptychographic microscope-----	13
1.3 The application of Fourier ptychographic microscope -----	16
2. Sparsely sampled Fourier ptychography -----	19
2.1 Introduction to the sparsely sampled Fourier ptychography -----	19
2.2 Analysis of the data redundancy requirement in FP-----	19
2.3 The principle of sparsely sampled Fourier ptychography-----	23
2.4 The principle of sparsely sampled Fourier ptychography-----	26
3. Spectral multiplexing and coherent-state decomposition in Fourier ptychographic imaging-----	30
3.1 Background- -----	30
3.2 State-multiplexed Fourier ptychography -----	30
3.3 Simulations and experiments of the state-multiplexed FP scheme-----	36
3.4 Spectral multiplexing in Fourier ptychographic imaging-----	41
4. High-resolution fluorescence imaging via pattern-illuminated Fourier ptychography-----	44
4.1 introduction and background-----	44
4.2 Pattern-illuminated Fourier ptychography-----	45
4.3 Simulations of the pattern-illuminated FP framework-----	49
4.4 Experimental demonstration of the pattern-illuminated FP approach-----	52

5. Field-portable high-resolution microscope using a cellphone lens-----	57
5.1 Introduction and background -----	57
5.2 System design of the FPscope-----	59
5.3 System characterization of the FPscope-----	61
5.4. Demonstration of the FPscope with biological samples-----	62
6. Conclusion-----	65
Reference -----	70

## Abstract

Fourier ptychographic (FP) imaging is a recently developed technique to get high-resolution high-throughput imaging. FP iteratively stitches together many variably illuminated, low-resolution intensity images in the Fourier space to expand the frequency passband and recover a high-resolution sample image.

There are several latest developments of the Fourier ptychographic imaging scheme. FP scheme can be used as adaptive imaging method. An image-quality metric is defined as a guide star for the optimization process, and system corrections are then performed to maximize such a guide star. The adaptive FP scheme performs system correction by modifying the complex transfer function in the recovery process, which can be used to recover the unknown pupil function, perform system correction and recover unknown system parameters.

To shorten the acquisition time of the FP platform, sparsely sampled FP, which uses a sparse-sampled mask to filter the captured intensity images, is developed and it reduced the acquisition time by  $\sim 50\%$ . In addition, the application of sub-sampled Fourier ptychography solved the pixel aliasing problem.

State-multiplexed FP, which allows the illumination of at most 4 LEDs at the same time, is able to shorten the acquisition time and the number of frames for 2~4 times. Similar reconstruction procedure is used to decompose R/G/B data and recovery a colorful high-resolution image, which can also be used to replace spectral filter, gratings or other optical components for spectral multiplexing and demultiplexing.

Pattern-illuminated FP extends the original FP from coherent imaging to incoherent imaging. Instead of using coherent light with different incident angles, pattern-illuminated FP uses different structured pattern to illuminate sample, and then recover a high resolution image.



Finally, based on the FP algorithm, a field-portable high-resolution microscope using a cellphone lens was design for low-cost imaging. It uses a cellphone lens in a reverse manner and a LED array as illumination. The FPscope can get a maximum synthetic numerical aperture (NA) of 0.5 and depth-of-focus of 0.1mm, which is longer than that of a conventional microscope objective with a similar NA.

## List of Figures

1.1 The FP setup and the recovery procedures (adapted from [9] and [11]). (a) An LED array is used to illuminate the sample with angle-varied plane waves. The objective's optical-transfer-function imposes a well-defined constraint in the Fourier domain. This constraint is digitally panned across the Fourier space to reflect the angular variation of angle-varied illuminations. (b) The iterative phase retrieval procedures of the FP. -----	14
1.2 Wide-field, high-resolution imaging via FP (adapted from [9]). FP combines the field-of-view advantage of a 2X objective and resolution advantage of a 20X objective. -----	16
1.3 Comparing FPM phase reconstructions to digital holographic and theoretical data. FPM transforms low-resolution intensity images from a 2 $\times$ objective (a1) into a high-resolution phase map (a2) of different-sized polystyrene microbeads, as compared with a DH reconstruction (a3) using a 40 $\times$ objective. (b) A similar image sequence highlights FPM's phase-imaging capabilities on a human blood smear. (c) Line traces through the microbeads and a RBC demonstrate quantitative agreement with expected phase performance. -----	17
2.1 FP reconstructions with different spectrum overlapping percentages. (a1)-(a2) Input high-resolution intensity and phase profiles of the simulated complex sample. (b)-(d) FP reconstructions with different spectrum overlapping percentages in the Fourier domain. (e) The RMS errors of the FP reconstructions versus the spectrum overlapping percentages. (a1) is copyrighted by MIT; we use it with permission. -----	20
2.2 FP reconstructions with different empty pixel percentages in the spatial domains. (a)-(c) FP reconstructions with 10%, 60%, and 90% empty pixels. (d) The RMS error of the FP reconstructions versus the empty pixel percentage. -----	22
2.3 The joint spectral-spatial sampling requirement of the FP recovery process. The RMS metric is plotted as a function of the spectrum overlapping percentage. Different curves represent cases with different empty pixel percentages. The FP convergence region is enclosed by the dark dash line. -----	23
2.4 (a1-a2) The overexposed raw images of a blood smear sample. (b1-b2) The corresponding HDR images of (a1) and (a2). Two exposure times were used in the HDR combination process. (c1-c2) The sparsely sampled masks raw images (a1) and (a2). -----	24
2.5 (a) The raw image of a blood smear sample. The FP reconstructions without (b) and with (c) the HDR combination process. (d) The reconstructions using the sparsely sampled FP scheme. (b1)-(c1) The recovered high-resolution intensity images. (b2)-(d2) The recovered high-resolution phase images. -----	26
2.6 (a) Pixel aliasing problem due to a large pixel size in the spatial domain. (b) The subsampled scheme by dividing one original pixel into 4 sub-pixels. The effective pixel size is only half of the original pixel size. At each iteration, only 1 out of 4 sub-pixels is updated by the measurement. The other 3 are kept unchanged. -----	27
2.7 Simulation of the sub-sampled FP scheme. (a) Raw intensity image with the pixel size larger than the Nyquist limit. (b1-b2) The FP reconstructions using the sub-sampled scheme. (b3) The recovered spectrum of (b1) and (b2). (c1-c2) The FP reconstructions without using the sub-sampled scheme. (c3) The recovered spectrum of (c1) and (c2). -----	28
2.8 Experimental validation of the sub-sampled FP scheme. (a) Raw intensity image with a pixel size (4.125 $\mu\text{m}$ ) larger than the Nyquist limit (3.15 $\mu\text{m}$ ). (b1) The FP reconstruction using the sub-sampled scheme. The linewidth of group 9 element 3 is 0.78 $\mu\text{m}$ . (b2) The recovered spectrum of (b1). (c1) The FP reconstruction without using the sub-sampled scheme. The image	

quality is significantly degraded by the pixel aliasing problem. (c2) The recovered spectrum of (c1).	29
3.1 The recovery procedures of the state-multiplexed Fourier ptychography scheme.	31
3.2 Simulations of the single-state and state-multiplexed FP schemes. (a1) and (a2) the input intensity and phase images of the simulated object. (b1) Raw data of the single-state FP scheme. Each low-resolution image (0.1 NA) corresponds to one LED element in the array. (b2) and (b3) the recovered sample intensity and phase images using the single-state FP scheme. (c1) Raw data of the state-multiplexed FP scheme. Two adjacent LED elements are lit up simultaneously for sample illumination, and each low-resolution intensity image (0.1 NA) represents an incoherent summation of two coherent states. (c2) and (c3) the recovered sample intensity and phase images (0.5 NA) using the state-multiplexed FP scheme. (d1) and (d2) the reconstructions of state-mixed raw data using the single-state FP scheme (for comparison).	33
3.3 Experiments of the single-state and state-multiplexed FP schemes. (a1) and (a2) The experimental setups for the two schemes. (b1) Raw data of the single-state FP scheme (0.1 NA). (b2) and (b3) The recovered sample intensity and phase images using the single-state FP scheme (0.5 NA). (c1) Raw data of the state-multiplexed FP scheme (0.1 NA). Two adjacent LED elements are lit up simultaneously for sample illumination, and each low-resolution intensity image represents an incoherent summation of two coherent states. (c2) and (c3) The recovered sample intensity and phase images using the state-multiplexed FP scheme (0.5 NA). (d1) and (d2) The reconstructions of state-mixed raw data using the single-state FP scheme (for comparison).	35
3.4 Color-multiplexed FP scheme. R/G/B LEDs are turned on simultaneously for illumination. Low-resolution images are acquired using a 0.1 NA objective lens and a monochrome camera. A color-multiplexed FP recovery algorithm is then used to decouple the R/G/B channels from the low-resolution images. A high-resolution color image of the sample can be recovered using computation instead of spectral filters.	37
3.5 Color-multiplexed FP recovery routine.	38
3.6 Simulations of the color-multiplexed FP scheme. (a) Input R/G/B channels and the color image. (b) The low-resolution intensity measurement of the object, representing an incoherent summation of 3 object profiles at different wavelengths. (c) The color-multiplexed FP recovery (0.5 NA). The mean-square errors for (c1)-(c3) are 0.5%, 0.4%, and 0.1%, respectively.	39
3.7 Experimental demonstration of the color-multiplexed FP scheme. (a) Raw data of the color-multiplexed FP acquisition, representing incoherent summation of the sample profiles at three wavelengths. (b1)-(b3) The recovered color-multiplexed high-resolution images (0.5 NA) at red, green, and blue channels. (c) The recovered color image by combining (b1)-(b3) (with white balance). (d) The recovered color image (0.5 NA) using three separated FP acquisitions with individual red, green, and blue illumination (no state-mixing). (e) Color image using a conventional microscope with a 40X high-NA objective lens (0.6 NA).	41
4.1 Overview of the pattern-illuminated FP recovery scheme. Multiple pattern-illuminated low-resolution images $I_n$ ( $n = 1, 2, 3, \dots$ ) are used to recover the high-resolution sample image $I_{obj}$ . In the last low-resolution image $I_n$ , the high-frequency illumination pattern is filtered out by the low-NA objective lens.	46
4.2 Flow chart of the pattern-illuminated FP algorithm.	47
4.3 Pattern-illuminated FP recovery using sinusoidal patterns. (a1) Simulated raw image without noise, and (a2) with 1% additive noise. (a3) The Fourier spectrum of (a1). FP recoveries using (b) 18 raw images, (c) 36 images, and (d) 54 images. We used 15 loops for the FP	

reconstructions. For the noise-free cases, the corresponding MSEs are 1.07%, 0.70%, and 0.44% for (b1)-(d1). For the cases with 1% noise, the corresponding MSEs are 1.65%, 1.30%, and 1.12% for (b2)-(d2). (e) The MSE is plotted as function of different noise levels. Different color lines correspond to different number of raw images. -----	50
4.4 Pattern-illuminated FP recovery using unknown patterns. (a) The unknown illumination pattern (random pattern) is translated into 169 different spatial positions. (b1) The simulated raw image. (b2) The Fourier spectrum of (b1). (c) The recovered illumination pattern. (d) The recovered high-resolution object image and its Fourier spectrum. We used 15 loops for the FP reconstructions. The MSE of (d1) is 0.4%. -----	52
4.5 (a) Pattern-illuminated FP setup. A diffuser is placed at the epi-illuminated arm of the microscope platform. The excitation light from the objective lens forms a speckle pattern on the sample. The resulting fluorescence emission from sample is then collected by the objective lens and detected by the CCD camera. (b1)-(b4) 4 acquired raw images. -----	53
4.6 Imaging performance of the pattern-illuminated FP approach. (a1) Sample image acquired using the 10X objective lens with uniform illumination. (b1) Speckle-illuminated raw image. (b2) FP recovery using 49 raw images. (c1) Sample image acquired using a 40X high-NA objective lens. (a2), (b3), (c2) Intensity lines traces of the highlighted features in (a1), (b2), (c1). For (a1) and (c1), we averaged multiple frames to get a similar photon budget as (b2). -----	54
4.7 FP reconstructions using different number of raw images. We used 5-9 loops for the iterative recovery process. (a) 9-frame recovery. (b) 16-frame recovery. (c) 25-frame recovery. (d) 49-frame recovery. (a1)-(d1) The recovered object profiles. (a2)-(d2) The recovered unknown illumination patterns. (a3)-(d3) Intensity lines traces corresponding to the highlighted features in (a1)-(d1). The FP reconstruction converges with 25 raw images. -----	55
5.1 System design of FPscope. (a) A cellphone lens is used in a reverse manner. The magnified sample image is projected onto a CCD sensor. An 8 by 8 LED matrix is used for sample illumination. (b) The assembled FPscope connected to a computer. -----	59
5.2 The assembling process of the FPscope. (a) A Nokia cellphone lens is fit in to a plastic case. (b) The case is assembled onto a CCD camera. (c) The assembling of the x-y stage and the slide holder. (d) The assembling of the z stage. (e) The final assembled FPscope. -----	60
5.3 Resolution characterization of the FPscope. (a) One of the 64 low-resolution raw images captured using the cellphone lens. (b) The FP recovered image, where feature of group 9, element 3 can be clearly resolved. -----	61
5.4 (a) Depth-of-focus characterization of the FPscope. One of the low-resolution raw images captured at (b1) $z = 50 \mu\text{m}$ and (c1) $z = -50 \mu\text{m}$ . (b2-b3), (c2-c3) The FP reconstructions by introducing a second-order defocused pupil function at the recovery process. The depth-of-focus is orders of magnitude longer than that of conventional microscope objective lens with similar NA. -----	62
5.5 (a) Rawimage of a blood smear (0.15 NA). FP recovered intensity image (b), phase (c), and color image (d). The maximum synthetic NA is 0.5. (e) The image captured using a conventional microscope with a 40X, 0.75 NA objective lens. -----	63
5.6 Demonstration of the FPscope using a pathology slide. The full field-of-view is about 1.2 mm by 0.9 mm. The maximum synthetic NA is 0.5. Images captured using conventional microscope with a 0.75 NA objective lens are also shown for comparison. -----	64

# Chapter 1

## Introduction

In an imaging platform, space-bandwidth product (SBP) is the fundamental limit to the throughput. SBP is defined as the number of degrees of freedom it can extract from an optical signal. In microscopy, the SBPs of most off-the-shelf objective lenses are on the order of 10 megapixels, regardless of their magnification factors or numerical apertures (NA). For example, a standard 20X microscope objective lens (MPLN 20X, 0.4 NA, Olympus) has a resolution of 0.8  $\mu\text{m}$  and a field-of-view with 1.1 mm diameter, corresponding to a SBP of  $\sim 8$  megapixels.

However, a large SBP is highly needed in pathology, hematology, immunohistochemistry and neuroanatomy. To solve this problem, commercial development of sophisticated mechanical scanning microscope systems and lensless imaging set-ups has been prompted to raise the SBP. But the disadvantage is that the mechanical scanning system requires precise control over actuation, optical alignment and motion tracking. Furthermore, it also neglects the computational addressable problem of resolution enhancement. Though lensless imaging gives a unique imaging capabilities, it still has some disadvantages. For instance, digital in-line holography does not work well for contiguous samples and contact-imaging microscope requires a sample to be very close to the sensor.

Fourier ptychography (FP) tackles this problem from another perspective. It is capable of providing a scalable SBP for most existing microscopes without involving mechanical scanning or phase measurements.

### 1.1 Introduction to Fourier ptychographic microscope

Fourier ptychography iteratively stitches together many variably illuminated, low-resolution intensity images in the Fourier space to expand the frequency passband and recover a high-

resolution complex sample image. Instead of directly measuring the phase information of the incoming light field, FP uses an iterative phase retrieval process to recover the complex phase information of the sample. It has been shown that, without involving any interferometry measurement and mechanical scanning, FP facilitates microscopic imaging well beyond the cutoff frequency set by the NA of the objective lens.

## 1.2 The principle of Fourier ptychographic microscope

A typical FP platform consists of an LED array and a conventional microscope with a low-NA objective lens, as shown in Fig. 1.1(a). The LED array is used to successively illuminate the sample at different incident angles (one LED element corresponds one incident angle). At each illumination angle, FP records a low-resolution intensity image of the sample. Under the thin-sample assumption, each acquired image uniquely maps to a different passband of the sample's spectrum.

The FP algorithm then recovers a high-resolution complex sample image by alternatively constraining its amplitude to match the acquired low-resolution image sequence, and its spectrum to match the panning Fourier constraint, as shown in Fig. 1.1(a). Essentially, FP introduces angular diversity functions to recover the high-resolution complex sample image, as compared to the translational diversity functions used in the conventional ptychography approach [1].

The reconstruction procedures of the FP are shown in Fig. 1.1(b). It starts with a high-resolution spectrum estimate of the sample:  $\widehat{U}_0(k_x, k_y)$ . This sample spectrum estimate is then sequentially updated with the low-resolution intensity measurements  $I_{im}$  (subscript 'm' stands for measurement and 'i' stands for the *i*th LED). For each update step, we select a small sub-region of the  $\widehat{U}_0(k_x, k_y)$ , corresponding to the optical-transfer-function of the objective lens,

and apply Fourier transformation to generate a new low-resolution target image  $\sqrt{I_{li}} e^{i\varphi_{li}}$  (subscript 'l' stands for low-resolution and 'i' stands for the *i*th LED). We then replace the target image's amplitude component  $\sqrt{I_{li}}$  with the square root of the measurement  $\sqrt{I_{mi}}$  to form an updated, low-resolution target image  $\sqrt{I_{mi}} e^{i\varphi_{li}}$ . This image is then used to update its corresponding sub-region of  $\widehat{U}_0(k_x, k_y)$ . The replace-and-update sequence is repeated for all intensity measurements, and we iterate through the above process several times until solution convergence, at which point  $\widehat{U}_0(k_x, k_y)$  is transformed to the spatial domain to produce a high-resolution complex sample image. The achievable resolution of the final FP reconstruction is determined by the latest incident angle of the LED array. As such, FP is able to bypass the design conflicts of conventional microscopes to achieve high-resolution, wide field-of view imaging capabilities.

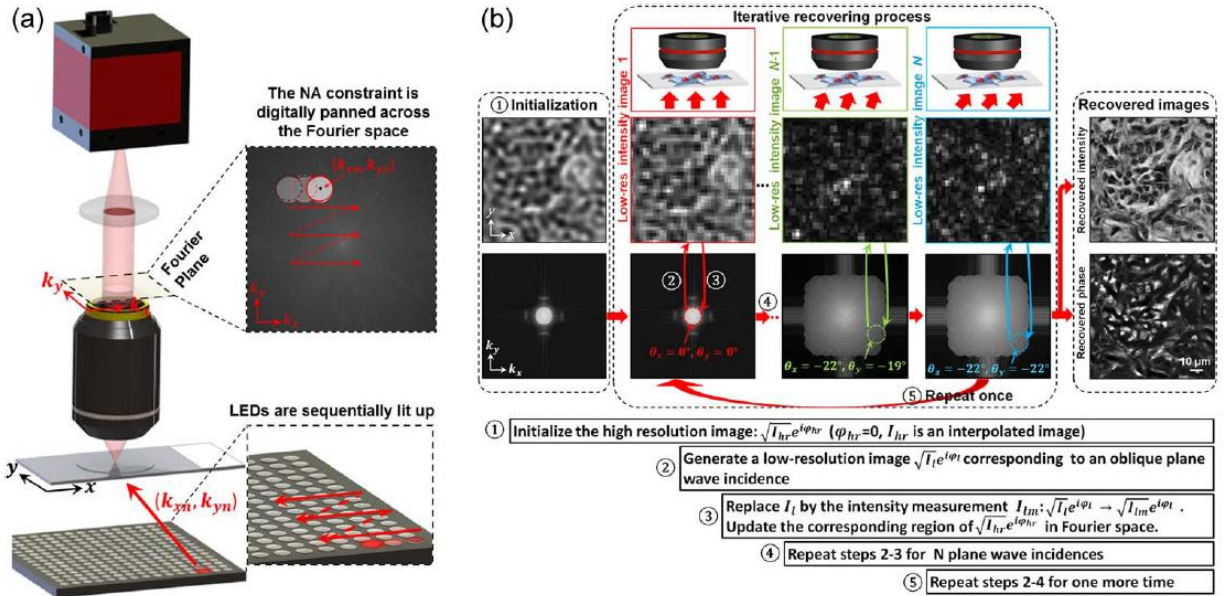


Fig. 1.1. The FP setup and the recovery procedures (adapted from [2] and [3]). (a) An LED array is used to illuminate the sample with angle-varied plane waves. The objective's optical-transfer-function imposes a well-defined constraint in the Fourier domain. This constraint is digitally panned across the Fourier space to reflect the angular variation of angle-varied illuminations. (b) The iterative phase retrieval procedures of the FP.

The name of Fourier ptychography comes from a related phase retrieval scheme, ptychography [3], [4]–[15]. Ptychography is lensless imaging approach originally proposed for

transmission electron microscopy [4] and brought to fruition by Faulkner and Rodenburg [5]. It uses a focused beam to illuminate the sample and records multiple diffraction patterns as a function of sample positions. This set of diffraction patterns is then used to invert the diffraction process and recover the complex sample profile following the iterative phase retrieval strategy. It is clear that FP and ptychography both share the strategy of phase retrieval technique: iteratively seeking a complex sample solution that is consistent with many intensity measurements. With ptychography, the object support constraints for phase retrieval are imposed by the confined illumination beam in the spatial domain. As such, the sample must be mechanically scanned through the desired field-of-view. With FP, on the other hand, the object support constraints are given by the confined optical-transfer function in the Fourier domain. In this regard, FP acts as the Fourier counterpart to ptychography, justifying its name [16]. By using a low-NA objective lens, FP naturally offers a large and fixed field of-view, high signal-to-noise ratio, and no mechanical scanning as compared to the conventional ptychography. The use of lens elements in FP settings also reduces the coherence requirement of the light source. Post-processing used in conjunction with the panning LED illuminations then leads to a resolution-improved, high-pixel-count final image. Furthermore, as discussed below, FP is able to digitally correct for aberrations and extend the depth-of-focus beyond the physical limitation of the objective lens.



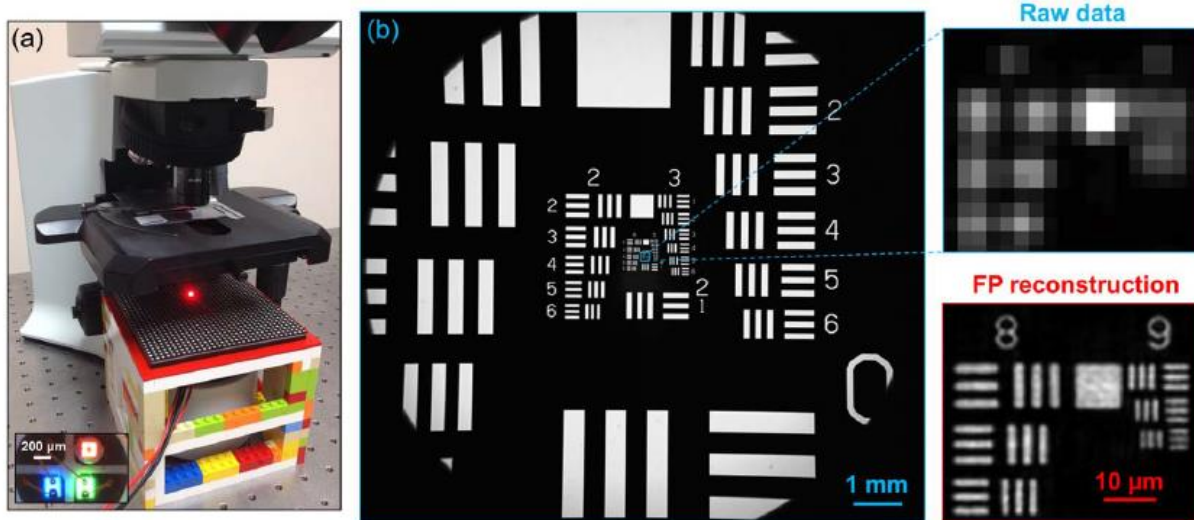


Fig. 1.2. Wide-field, high-resolution imaging via FP (adapted from [2]). FP combines the field-of-view advantage of a 2X objective and resolution advantage of a 20X objective.

### 1.3 The application of Fourier ptychographic microscope

Fourier ptychographic microscope is a wide-field, high-resolution, long depth-of-focus imaging method. This technique may potentially free clinicians from bowing in front of the microscope and manually moving the sample to different regions for observation. As digital imaging is introduced to laboratory environment, it may also have the potential to improve the work environment and laboratory productivity, to enable education, and to enhance communication and collaboration between clinicians.

In addition, as Fourier ptychographic imaging is also a phase retrieval imaging method. Many biological samples do not absorb or scatter light significantly. As such, they are transparent or generate little contrast under a conventional bright-field microscope. FP is able to recover both the intensity and phase of an optical field exiting a sample, which is shown in figure 1.3. Therefore, it holds a great potential for quantitative image analysis. Therefore, it holds a great potential for quantitative image analysis.

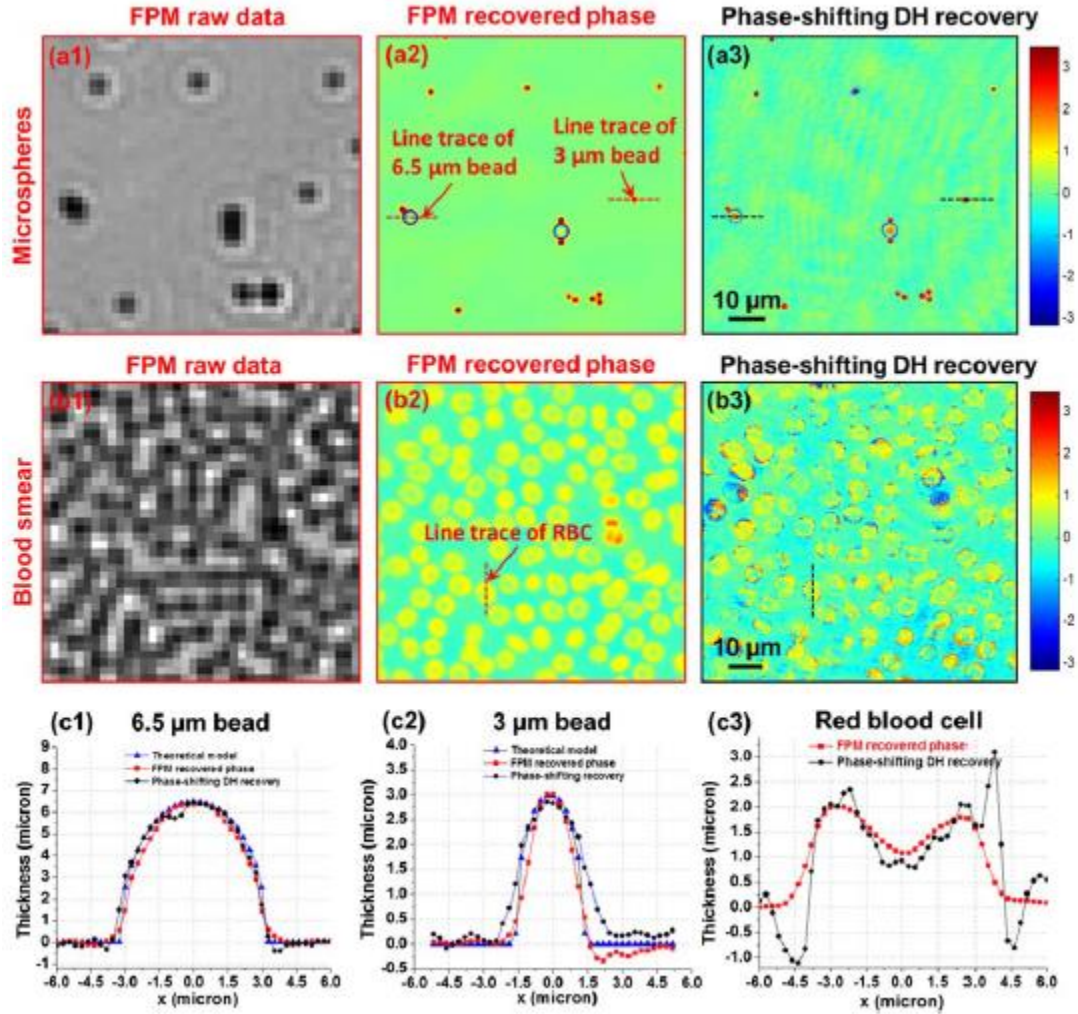


Fig. 1.3. Comparing FPM phase reconstructions to digital holographic and theoretical data. FPM transforms low-resolution intensity images from a  $2\times$  objective (a1) into a high-resolution phase map (a2) of different-sized polystyrene microbeads, as compared with a DH reconstruction (a3) using a  $40\times$  objective. (b) A similar image sequence highlights FPM's phase-imaging capabilities on a human blood smear. (c) Line traces through the microbeads and a RBC demonstrate quantitative agreement with expected phase performance.

The concepts in adaptive optics [17]–[19] can also be implemented in the FP scheme to perform adaptive Fourier ptychographic imaging [20]. In the adaptive FP scheme, an image-quality metric is defined as a guide star for the optimization process, and system corrections are then performed to maximize such a guide star. Compared to conventional adaptive imaging systems, the adaptive FP scheme performs system corrections by modifying the complex transfer function in the iterative recovery process (no adaptive optical hardware is needed), offering a unique advantage on system simplicity and reliability. We demonstrates the use of the adaptive

FP to recover the unknown pupil function and perform aberration correction. Such a scheme can also be used to correct for intensity uncertainty of the LED array and recover unknown system parameters [20].

## Chapter 2

### Sparsely sampled Fourier ptychography (Adapted from [27])

#### 2.1 Introduction to the sparsely sampled Fourier ptychography

A key aspect of a successful FP reconstruction is the data redundancy requirement of the recovery process. In particular, such a data redundancy requirement is important for recovering the ‘lost’ phase information of the sample. So analysis of data redundancy both in spatial domain and Fourier domain is important to the amount of raw images needed to capture. Based on the conclusion, a sparsely sampled FP scheme by selectively updating the pixel values in the spatial domain is used to bypass the HDR combination process in the original FP platform, which can shorten the acquisition time of the FP platform by ~50%.

#### 2.2 Analysis of the data redundancy requirement in FP

In a FP experiment, the interaction between a plane wave illumination and a sample can be modeled as  $t(x, y)e^{ik_{xi}x + ik_{yi}y}$ , when  $t(x, y)$  is the complex transmitted function of the sample, and  $e^{ik_{xi}x + ik_{yi}y}$  is a plane illumination with a wavevector  $(k_{xi} + k_{yi})$ . Multiplication of the plane wave illumination in the spatial domain is equivalent to shifting the sample spectrum in the Fourier domain. Thus, images with different plane wave illuminations correspond to different spectrum regions in the Fourier space. Intuitively, a certain amount of spectrum overlapping in between successive acquisitions is needed to connect all acquired images in the Fourier space. If there is no overlapping in between these spectrum regions, FP reduces to a conventional phase retrieval procedure where each image can be processed independently. In this section, the spectrum overlapping requirement of the FP recovery process is investigated. Specifically, how much spectrum overlapping is needed for a successful FP reconstruction?

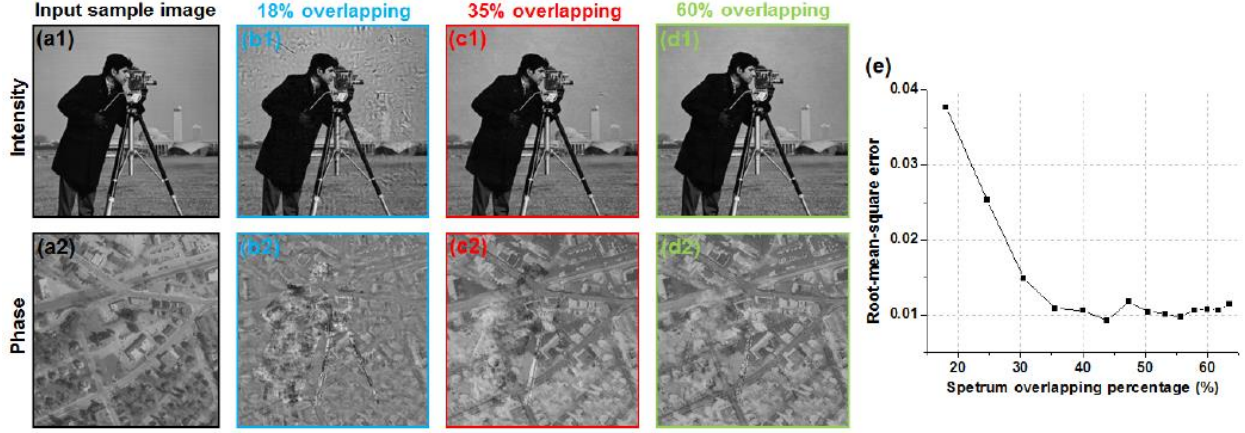


Fig. 2.1. FP reconstructions with different spectrum overlapping percentages. (a1)-(a2) Input high-resolution intensity and phase profiles of the simulated complex sample. (b)-(d) FP reconstructions with different spectrum overlapping percentages in the Fourier domain. (e) The RMS errors of the FP reconstructions versus the spectrum overlapping percentages. (a1) is copyrighted by MIT; we use it with permission.

The spectrum overlapping percentage is determined by the angular variation in between two successive illuminations. It is defined as the overlapping spectral region of two successive acquisitions divided by the entire region of the objective's pupil function. A typical FP platform uses an LED array for providing angle-varied illuminations. As such, the spectrum overlapping percentage is determined by the size of the LED element and the distance between the LED array and the sample. In Fig. 2.1, we investigate the spectrum overlapping requirement using simulations. The simulation parameters were chosen to realistically model a light microscope experiment, with an incident wavelength of 632 nm, a pixel size of  $2.75 \mu\text{m}$  and an objective NA of 0.08. We simulated the use of a  $15 \times 15$  LED array for illuminating the sample with different incident angles. Different spectrum overlapping ratio was achieved by adjusting the distance between the LED array and the sample.

The high-resolution input intensity and phase profiles are shown in Fig. 2.1(a1) and 2.1(a2), which serve as the ground truth of the simulated complex object. We then simulated the low-resolution measurements under different incident angles by imposing a low-pass filter at the corresponding regions of the Fourier space. These low-resolution images were then used to reconstruct the high-resolution complex sample image following the FP recovery procedures [2, 20]. Figure 2.1(b)-2.1(d) demonstrate the FP reconstructions under different spectrum overlapping percentages. It is obvious that the reconstruction quality of Fig. 2.1(b) (with an 18% overlapping percentage) is worse than those with

higher overlapping percentages. The image qualities of different FP reconstructions are quantified in Fig. 2.1(e), where root-mean-square (RMS) errors (i.e., the difference between the ground truth and the recovered images) are plotted as a function of the spectrum overlapping percentage. It is shown that the RMS errors decreases as the spectrum overlapping percentage increases, and a minimum of ~35% overlapping percentage is needed for a successful FP reconstruction.

After analysis of sampling in the Fourier domain, the sampling in the spatial domain is also investigated. The FP recovery process uses the amplitudes of the acquired images to constraint the high-resolution reconstruction in the spatial domain. In order to discuss the sampling requirement in the spatial domain, we first review the amplitude updating process in the FP algorithm. The FP algorithm starts with a high-resolution spectrum estimate of the sample. For each illumination angle, we select a small sub-region of this spectrum and perform inverse Fourier transform to generate a low-resolution target image. The amplitude component of this target image is then replaced by that of the acquired image while the phase component is kept unchanged. This amplitude updating process is repeated for all intensity measurements and we iterate through the process several times until solution convergence. This section is about how many pixels need to be updated in the spatial domain for a successful FP reconstruction.

The simulation parameters are the same as those of the previous section. We introduce a sparsely sampled mask in the updating process, as shown in Fig. 2.2(a3)-2.2(c3). This mask contains only two types of pixel values: 0 and 1. The regions corresponding to value '1' are updated as the original FP algorithm, while those corresponding to '0' are kept unchanged in the updating process. The pixel with value '0' is termed empty pixel. Figure 2.2(a1)-2.2(c1) and 2.2(a2)-(c2) demonstrate the recovered FP images with different empty pixel percentages. We can see that the reconstruction quality of Fig. 2.2(c) (with 90% empty pixels) is worse than those with lower empty pixel percentages. We also quantified the FP reconstruction qualities using the RMS error metric in Fig. 2.2(d). It is shown that, FP algorithm is able to recover the complex image with a maximum of ~70% of empty pixels.



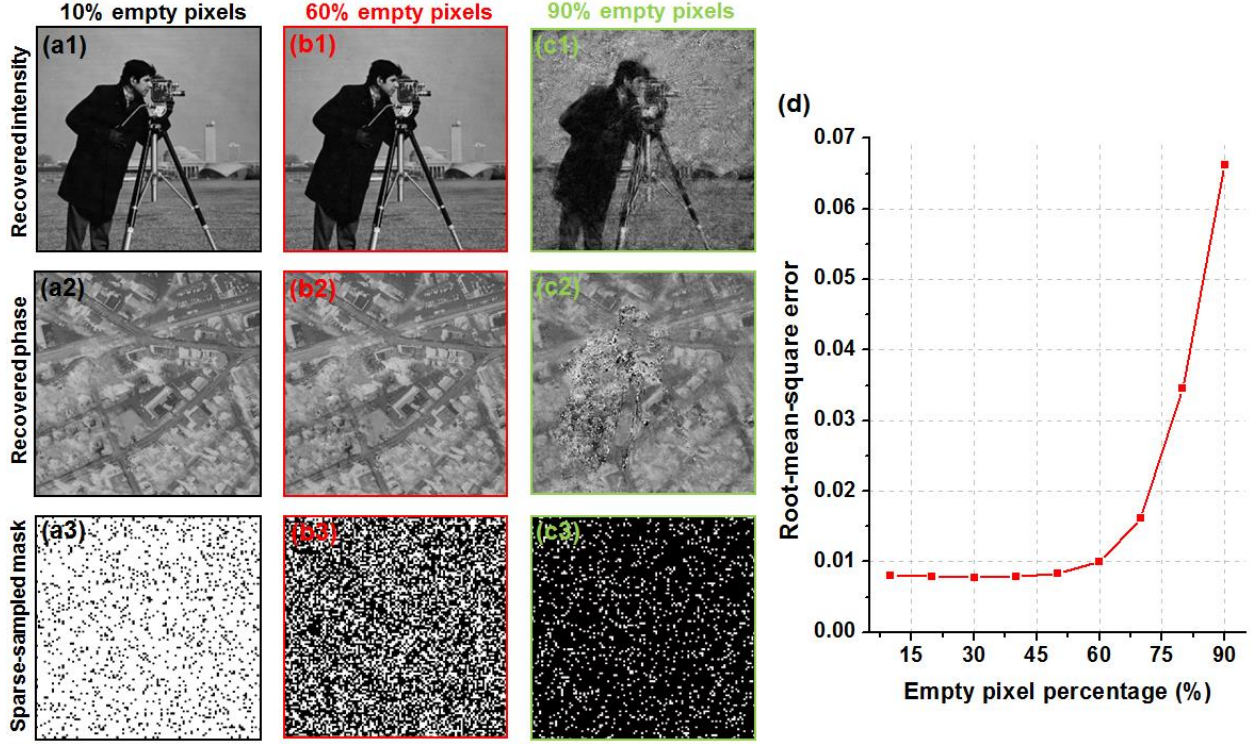


Fig. 2.2. FP reconstructions with different empty pixel percentages in the spatial domains. (a)-(c) FP reconstructions with 10%, 60%, and 90% empty pixels. (d) The RMS error of the FP reconstructions versus the empty pixel percentage.

In Fig. 2.3, we further analyze the joint spectral-spatial sampling requirement of the FP recovery process. Different curves in Fig. 2.3 represent different empty pixel percentages. The convergence region is enclosed by the dash line at the bottom right. It is shown that, a higher spectral sampling percentage results in a low spatial sampling requirement. The interplay between the spectral and spatial sampling requirements gives us more flexibility on designing the FP imaging platforms. For example, we can tradeoff the spatial sampling by using more LED illuminations. In the following two sections, we will demonstrate two application examples on exploring such a spectral-spatial sampling interplay.

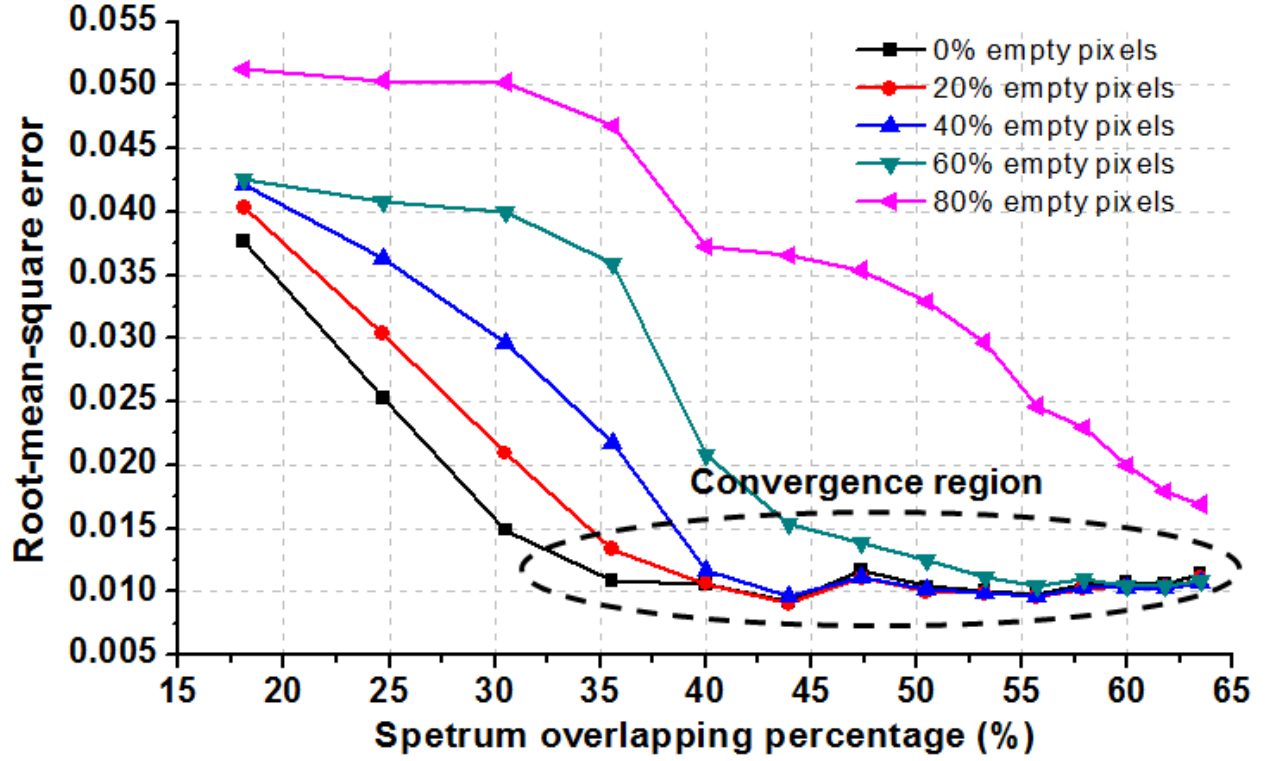


Fig. 2.3. The joint spectral-spatial sampling requirement of the FP recovery process. The RMS metric is plotted as a function of the spectrum overlapping percentage. Different curves represent cases with different empty pixel percentages. The FP convergence region is enclosed by the dark dash line.

### 2.3 The principle of sparsely sampled Fourier ptychography

As discussed above, the sampling interplay between the spectral and the spatial domains allows one to tradeoff the spatial sampling with an increased number of illuminations. In this section, we will report a sparsely sampled scheme following such a strategy. The reported scheme is able to bypass the HDR combination process in the original FP platform, and shorten the acquisition time considerably.



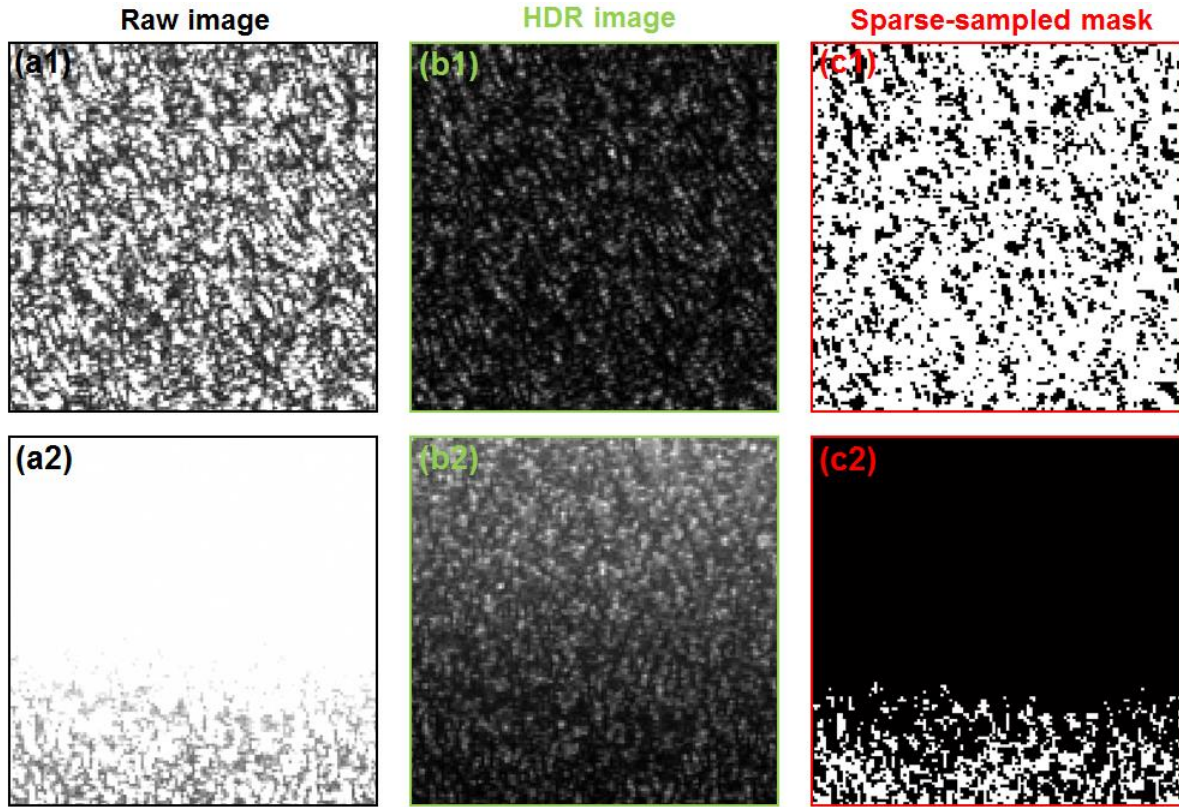


Fig. 2.4. (a1-a2) The overexposed raw images of a blood smear sample. (b1-b2) The corresponding HDR images of (a1) and (a2). Two exposure times were used in the HDR combination process. (c1-c2) The sparsely sampled masks by binarizing the overexposed raw images (a1) and (a2).

As demonstrated in Ref [2], a typical FP platform needs to acquire multiple images of the same scene with different exposure times (normally, one short and one long exposure are needed). These raw images are then combined to produce a HDR image of the scene. Figures .2.4(a1)-2.4(c1) and Figs. 2.4(a2)-2.4(c2) demonstrate two examples of such a HDR combination process. Figure 2.4(a1) and 2.4(a2) are two different raw images of the same blood smear sample, where many regions are overexposed. Figure 2.4(b2) and 2.4(b2) demonstrate the reconstructed images following the HDR combination step.

The principle of the sparsely sampled FP is straight forward. In the amplitude updating process, it produces a sparsely sampled mask by binarizing the overexposed raw image, as shown in Fig. 2.4(c1) and 2.4(c2). This mask is then imposed in the amplitude updating process: the regions with overexposed pixels will be kept unchanged while other regions will be updated

by the intensity measurement. Depending on the empty pixel percentage, one may need to increase the number of plane wave illuminations to ensure the solution convergence.

In a typical microscope experiment, the percentage of overexposed pixels is no more than 15%, and thus, the solution convergence condition withstands.

We validated the sparsely sampled FP scheme using a light microscope experiment. The experimental geometry was similar to that of simulation and we used the blood smear slide as our sample, the same as that of Fig. 8. Figure 2.5(a) show the raw image of the sample with a pixel size of  $2.75\ \mu\text{m}$ . Figure 2.5(b1) and 2.5(b2) are the recovered intensity and phase images without using the HDR combination process. These two FP reconstructions are corrupted by the overexposed pixels in the raw images. Figure 2.5(c1) and 2.5(c2) are the recovered images using the HDR combination process. The corresponding acquisition time is about 3 minutes (450 images in total). The results of the proposed sparsely sampled FP are shown in Fig. 2.5(d1) and 2.5(d2), and the corresponding acquisition time is about 1.6 minute (225 images in total). From the comparisons shown in Fig. 2.5, we can see that the image quality of the reported scheme is comparable to that of the original FP with the HDR combination step. The advantage of the reported scheme is obvious: it gets rid of the multi-exposure acquisition process and shortens the acquisition time by ~50%.

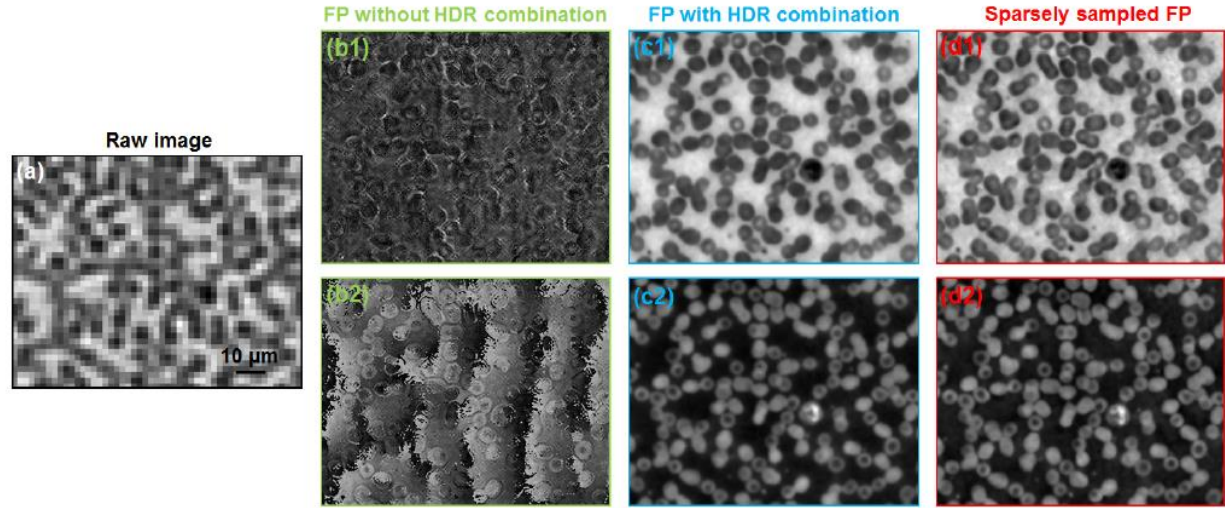


Fig. 2.5. (a) The raw image of a blood smear sample. The FP reconstructions without (b) and with (c) the HDR combination process. (d) The reconstructions using the sparsely sampled FP scheme. (b1)-(c1) The recovered high-resolution intensity images. (b2)-(d2) The recovered high-resolution phase images.

## 2.4 The principle of sparsely sampled Fourier ptychography

In a FP platform, the pixel size of the image sensor needs to be carefully chosen to match the optical transfer function of the objective lens. Nyquist theorem dictates that, the pixel size needs to be smaller than  $\lambda/(2 \cdot \text{NA})$ , where  $\lambda$  is wavelength of the light field and NA is the numerical aperture of the objective lens (the magnification factor is normalized in our discussion). A pixel size larger than this Nyquist limit may lead to the pixel aliasing problem in the Fourier domain (Fig. 2.6(a)). It will also significantly degrade the quality of the FP reconstruction. In this section, we will report a sub-sampled scheme, a special case of the sparsely sampled FP, to address the pixel aliasing problem. It is also important to acknowledge that, a similar updating procedure has been discussed in the lensless ptychography approach [13].

The sub-sampled FP scheme is shown in Fig. 2.6(b). We divide one original pixel into 4 sub-pixels, and thus, the effective pixel size is only half of the original pixel size. We then generate a sub-sampled mask in the amplitude updating step, as shown in the left part of Fig. 2.6(b). Only 1 out of 4 sub-pixels is updated by the measurement and the other 3 sub-pixels are

kept unchanged in the updating process. Essentially, this scheme is a special case of the sparsely sampled FP, with a 75% empty pixel percentage and a pre-defined sub-sampled mask.

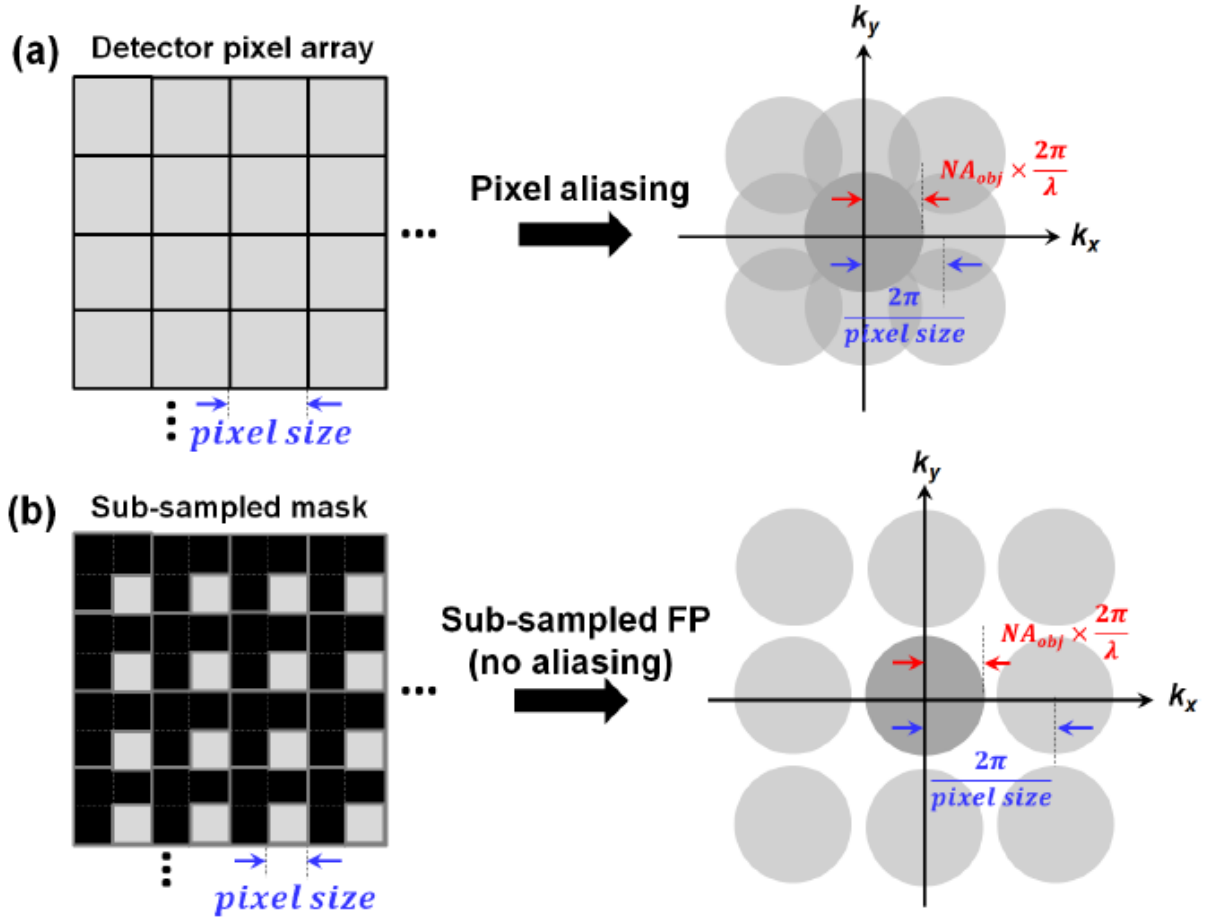


Fig. 2.6. (a) Pixel aliasing problem due to a large pixel size in the spatial domain. (b) The subsampled scheme by dividing one original pixel into 4 sub-pixels. The effective pixel size is only half of the original pixel size. At each iteration, only 1 out of 4 sub-pixels is updated by the measurement. The other 3 are kept unchanged.

We first validate this scheme using simulations. We chose a pixel size of  $4.125 \mu\text{m}$ , a wavelength of  $0.63 \mu\text{m}$ , and a NA of 0.1. Therefore, the pixel size is larger than the Nyquist limit of  $3.15 \mu\text{m}$ . We simulated the use of a  $15 \times 15$  LED array for illuminating the sample from different incident angles. The spectrum overlapping percentage is  $\sim 65\%$ . Figure 2.7(a) shows one raw intensity image of the sample. Figures 2.7(b1)-2.7(b2) demonstrate the FP reconstructions using the sub-sampled mask in the updating process. Figure 2.7(b3) shows the corresponding recovered spectrum in the Fourier space. Due to the pixel aliasing problem, there

is not enough bandwidth to impose the circular pupil function in the Fourier space. As such, each low-resolution image in Fig. 2.7(b3) corresponds to a square region in the Fourier space. The case without using the sub-sampled mask is shown in Figs. 2.7(c1)-2.7(c3), where the reconstructions are corrupted by the pixel aliasing problem.

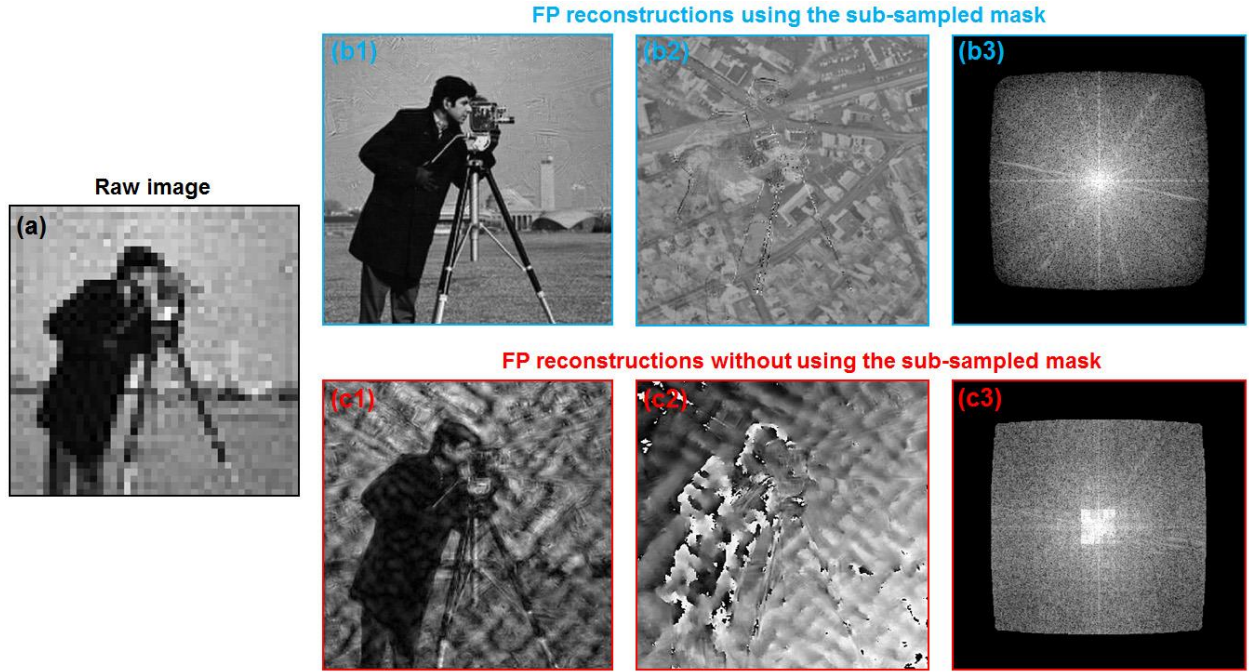


Fig. 2.7. Simulation of the sub-sampled FP scheme. (a) Raw intensity image with the pixel size larger than the Nyquist limit. (b1-b2) The FP reconstructions using the sub-sampled scheme. (b3) The recovered spectrum of (b1) and (b2). (c1-c2) The FP reconstructions without using the sub-sampled scheme. (c3) The recovered spectrum of (c1) and (c2).

We then validated the sub-sampled FP scheme using a light microscope experiment. The experimental setting was the same as the simulation, and a USAF resolution target was used as the sample. Figure 2.8(a) shows the raw intensity image of the sample. Figure 2.8(b1) and 2.8(b2) are the recovered high-resolution image and spectrum using the sub-sampled scheme. The FP reconstructions without using the sub-sampled scheme are shown in Fig. 2.8(c1) and 2.8(c2). It is obvious that, the sub-sampled FP scheme is able to reconstruct an artifact-free sample image. On the other hand, the FP reconstructions without using the sub-sampled mask are corrupted by the pixel aliasing problem.



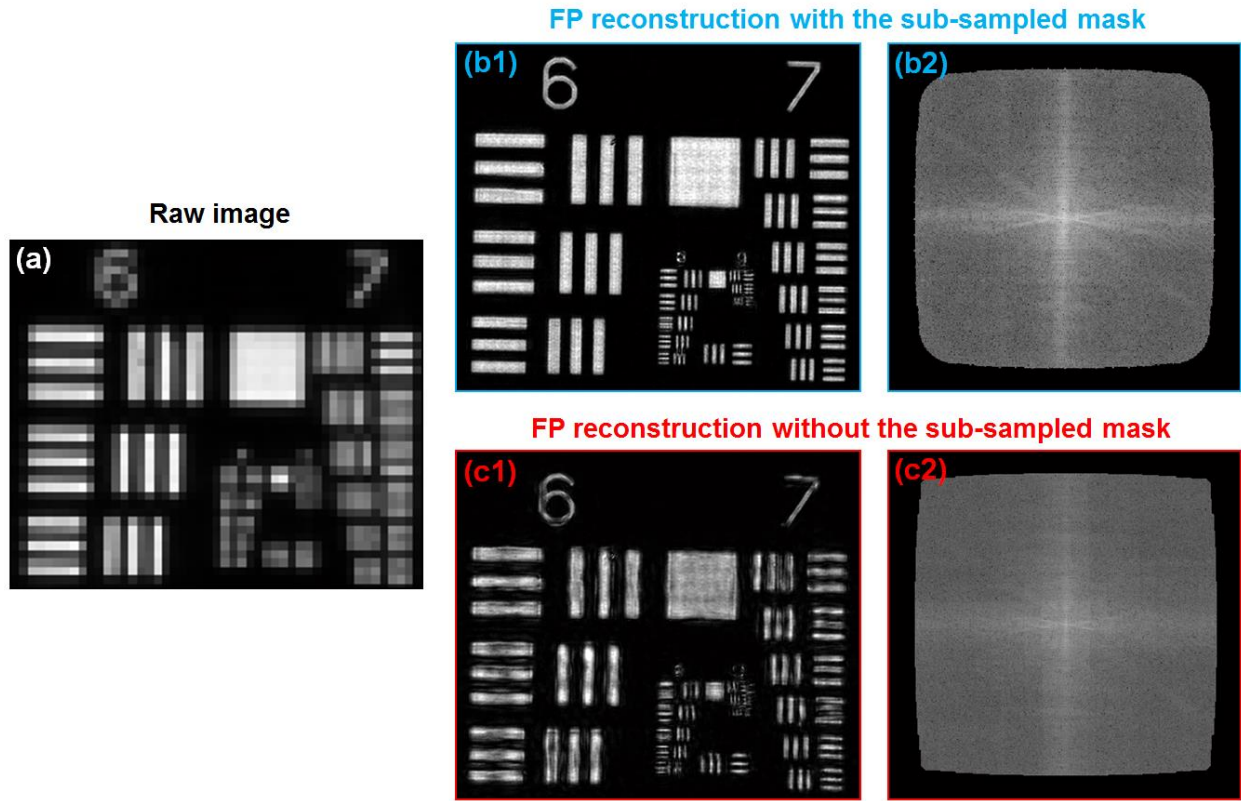


Fig. 2.8. Experimental validation of the sub-sampled FP scheme. (a) Raw intensity image with a pixel size ( $4.125 \mu\text{m}$ ) larger than the Nyquist limit ( $3.15 \mu\text{m}$ ). (b1) The FP reconstruction using the sub-sampled scheme. The linewidth of group 9 element 3 is  $0.78 \mu\text{m}$ . (b2) The recovered spectrum of (b1). (c1) The FP reconstruction without using the sub-sampled scheme. The image quality is significantly degraded by the pixel aliasing problem. (c2) The recovered spectrum of (c1).

## Chapter 3

### Spectral multiplexing and coherent-state decomposition in Fourier ptychographic imaging (Adapted from [58])

#### 3.1 Background

Despite the successful demonstration of the FP approach, its operation is currently limited to the single coherent state of the light source. In other words, the light source in FP settings is assumed to be spatially a point source and temporally a single wavelength. Incoherent mixture of multiple coherent states has not been considered in the FP recovery procedures. Therefore, one important step for advancing the FP technique is to develop a recovery scheme for handling state mixture and performing information multiplexing with FP acquisitions. As we will discuss later, such a state-multiplexed FP scheme may find applications in coherent-state decomposition and computational multispectral imaging.

Recently, mode expansion of the mutual coherence function has been reported for coherent diffractive imaging, which allowed reconstruction using partially coherent light sources [22–24]. A mixed-state formulation has also been reported for the lensless ptychography approach by Thibault and Menzel [25], and was recently applied to information multiplexing by Batey et.al [26]. Motivated by the previous works, in particular, the mixed state formulation of lensless ptychography [25], we report a state-multiplexed recovery scheme for Fourier ptychographic imaging settings. We validate the reported scheme with both simulations and experiments.

#### 3.2 State-multiplexed Fourier ptychography

A typical FP platform consists of an LED array, a conventional microscope with a low-NA objective lens, and a monochromatic CCD camera. The LED elements on the array are turned on sequentially to illuminate the sample from different incident angles. At each

illumination angle, the camera acquires a low-resolution intensity image of the sample. These acquired images are then stitched with overlap in the Fourier domain using the single-state FP algorithm.

In such a single-state FP algorithm, the generated low-resolution target images uniquely map to different regions of the sample estimate in the Fourier space. This one-to-one mapping relationship is a direct consequence of the single-coherent-state assumption, i.e., the illumination is assumed to be a point source spatially and a single wavelength temporally. In the case of low-coherent Fourier ptychographic acquisition, the intensity measurement represents an incoherent summation of different coherent states [25], and thus, the mapping between the low-resolution target image and the high-resolution sample estimate is not in a one-to-one relationship. In the reported state-multiplexed FP scheme, we model the decoherent effect using multiple target images, corresponding to different coherent states of the light source [25].

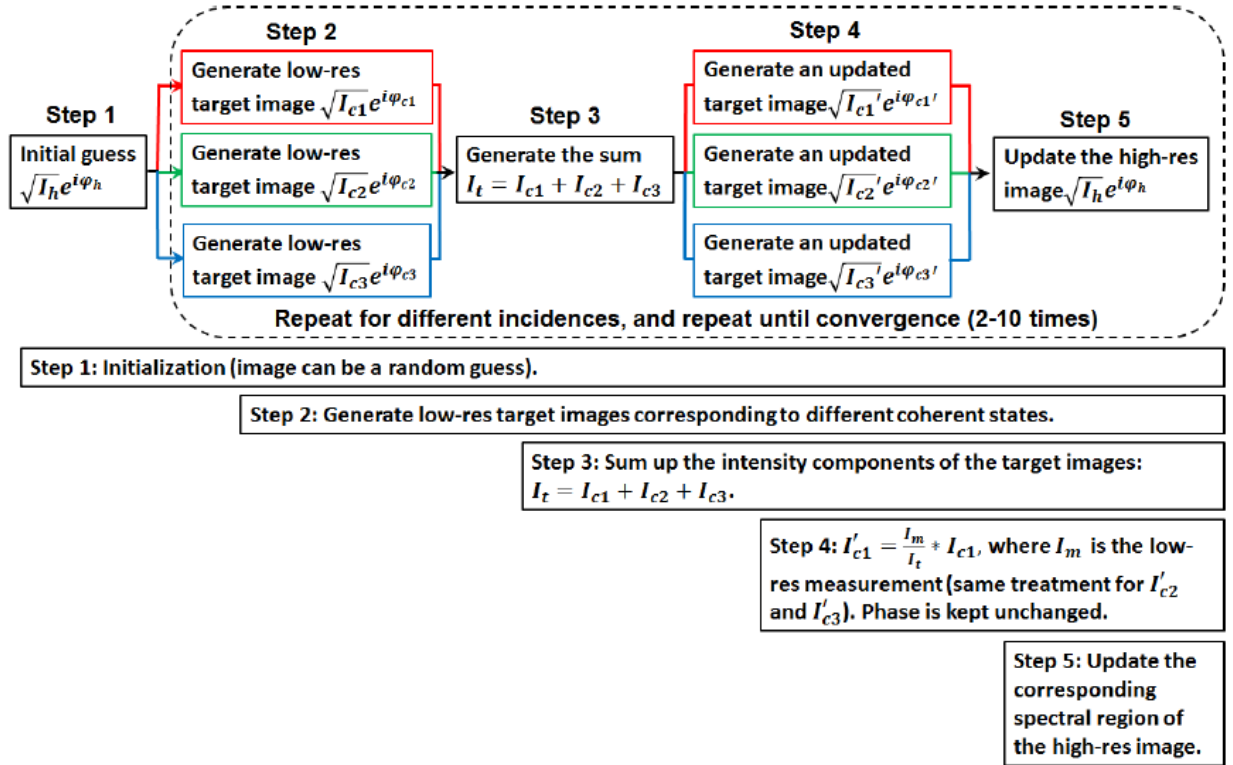


Fig. 3.1. The recovery procedures of the state-multiplexed Fourier ptychography scheme.



The recovery process of the state-multiplexed FP scheme is shown in Fig. 3.1. Similar to the single-state scheme, it starts with a high-resolution estimate of the sample profile:  $\sqrt{I_h}e^{i\varphi_h}$ . This sample estimate is used to generate multiple low-resolution target images corresponding to different coherent states. Second, the intensity components of the target images are summed up to generate the incoherent mixture  $I_t$ . Third, the ratio between the actual measurement  $I_m$  and  $I_t$  is used to update the intensity components of the target images, while the phase components are kept unchanged. Fourth, the updated target images are used to modify the corresponding spectral regions of the sample estimate. Lastly, the entire process is repeated for all intensity measurements, and iterated for several times until the solution converges. The computational cost of the state-multiplexed FP scheme is linearly proportional to the number of coherent states. For example, the computational time of two-state multiplexing is twice of the single-state's computational time. The key difference between the reported scheme and the single-state FP lies in the intensity replacement process. In the single-state FP, the intensity component of the target image is directly replaced by the actual measurement  $I_m$  while the phase component is kept unchanged. The reported state-multiplexed scheme, on the other hand, uses the ratio between the incoherent mixture and the actual measurement to update the intensity components of the target images. This new updating process ensures that the intensity summation of different coherent modes equates to the measured incoherent mixture, while the phase of individual modes is preserved.

### 3.3 Simulations and experiments of the state-multiplexed FP scheme

We first validated the state-multiplexed scheme using simulations. The simulation parameters were chosen to realistically model a light microscope experiment, with an incident wavelength of 632 nm, a pixel size of 1.375  $\mu\text{m}$  (at the sample plane) and an objective NA of 0.1

(Olympus 4X Plan). We simulated the use of a  $15 \times 15$  LED (SMD 3528) array for illuminating the sample with different incident angles. The LED array is placed 85 mm beneath the sample, and the distance between adjacent LEDs is 4 mm.

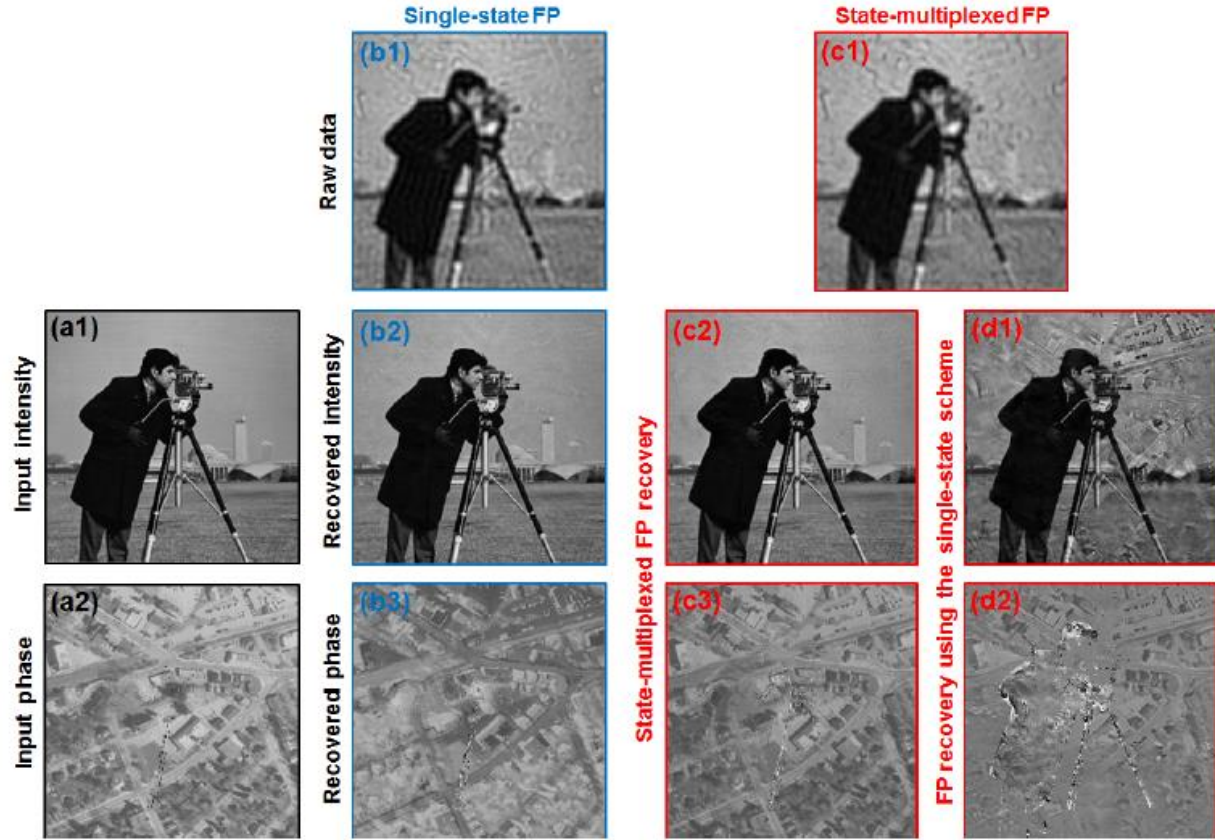


Fig. 3.2. Simulations of the single-state and state-multiplexed FP schemes. (a1) and (a2) the input intensity and phase images of the simulated object. (b1) Raw data of the single-state FP scheme. Each low-resolution image (0.1 NA) corresponds to one LED element in the array. (b2) and (b3) the recovered sample intensity and phase images using the single-state FP scheme. (c1) Raw data of the state-multiplexed FP scheme. Two adjacent LED elements are lit up simultaneously for sample illumination, and each low-resolution intensity image (0.1 NA) represents an incoherent summation of two coherent states. (c2) and (c3) the recovered amplitude and phase images (0.5 NA) using the state-multiplexed FP scheme. (d1) and (d2) the reconstructions of state-mixed raw data using the single-state FP scheme (for comparison).

The high-resolution input intensity and phase profiles are shown in Fig. 3.2(a1) and (a2), which serve as the ground truth for the simulated complex object. We then simulated the low-resolution measurements for 1) the single-state FP scheme and 2) the state-multiplexed FP scheme. For the single-state scheme, each low-resolution intensity image corresponds to one LED element in the array (225 images), as shown in Fig. 3.2(b1). The corresponding

reconstructed intensity and phase images are shown in Fig. 3.2(b2) and 3.2(b3). For the state-multiplexed scheme, we simulated the case of two adjacent LED elements lighting up simultaneously for sample illumination. In this case, each low-resolution intensity image (Fig. 3.2(c1)) represents an incoherent summation of two coherent states. As we group two LEDs as one light source element, the total number of simulated low-resolution images reduces by half (113 images; we did not group the last LED element). We note that, the spectrum-overlapping percentage (i.e., the data redundancy requirement) is determined by the distance between two adjacent light sources. In this case, two LEDs can be viewed as one ‘larger’ light source element, and the resulting averaged spectrum-overlapping percentage is determined to be ~55%, satisfying the convergence condition of ~40% [27]. Based on the simulated low-resolution state-mixtures, we applied the state-multiplexed FP scheme to recover the high-resolution sample images in Fig. 3.2(c2) and 3.2(c3). Using the state-mixture data set, we also used the single-state FP scheme (for comparison purpose) to reconstruct the sample images in Fig. 3.2(d1) and 3.2(d2).

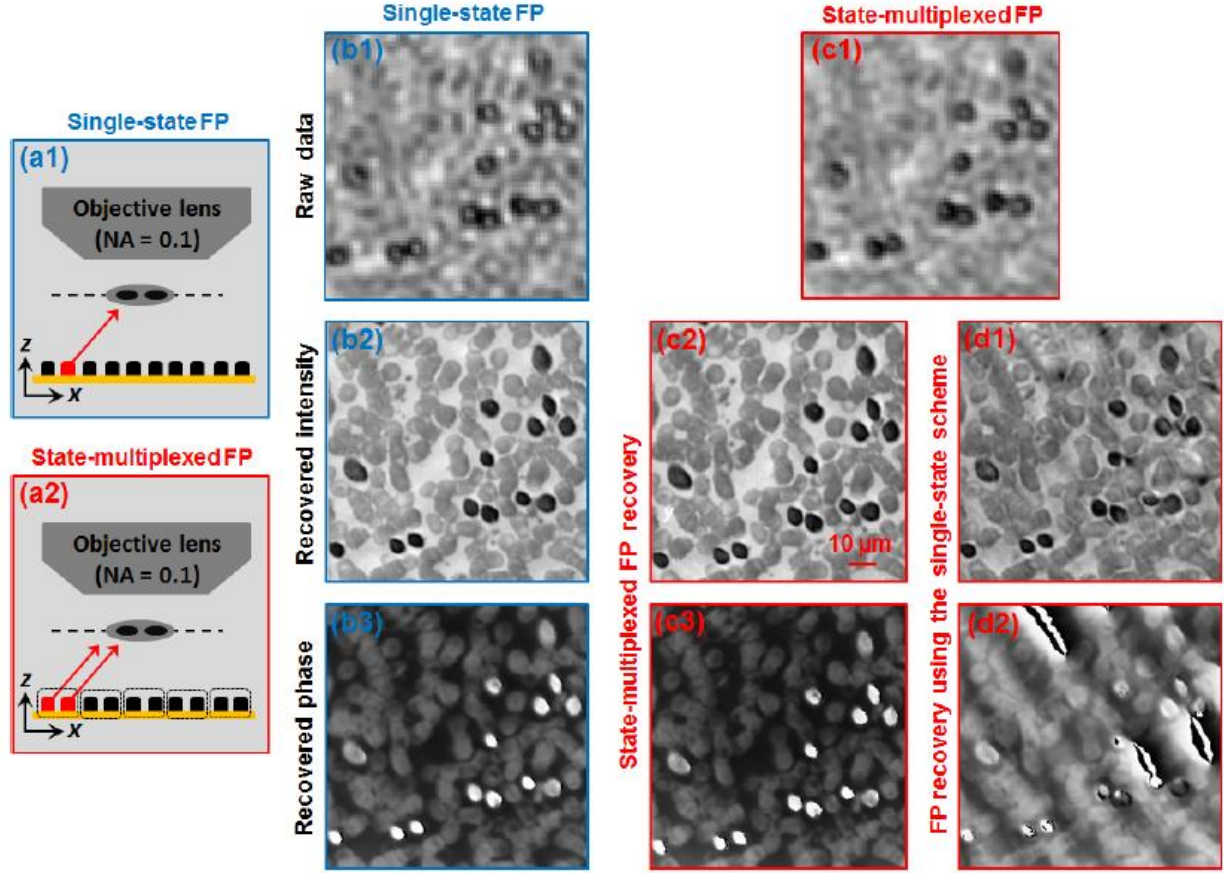


Fig. 3.3. Experiments of the single-state and state-multiplexed FP schemes. (a1) and (a2) The experimental setups for the two schemes. (b1) Raw data of the single-state FP scheme (0.1 NA). (b2) and (b3) The recovered sample intensity and phase images using the single-state FP scheme (0.5 NA). (c1) Raw data of the state-multiplexed FP scheme (0.1 NA). Two adjacent LED elements are lit up simultaneously for sample illumination, and each low-resolution intensity image represents an incoherent summation of two coherent states. (c2) and (c3) The recovered sample intensity and phase images using the state-multiplexed FP scheme (0.5 NA). (d1) and (d2) The reconstructions of state-mixed raw data using the single-state FP scheme (for comparison).

The image qualities of different FP reconstructions are quantified using the mean-square errors (the difference between the FP reconstructions and the ground truth; smaller errors represent better reconstruction). The mean-square errors for Fig. 13(b2), 13(c2), and 13(d1) are 0.11%, 0.47% and 4.0%, respectively. From this set of simulations, we can see that, the reported state-multiplexed scheme is able to recover the sample image with quality similar to single-state FP.

We next validated the state-multiplexed FP scheme using a light microscope experiment, as shown in Fig. 3.3. The parameters of the experimental setup are similar to those of

simulations. For the single-state FP scheme (Fig. 3.3(a1)), each acquired image corresponds to illumination from one LED element. Figure 3.3(b1) shows an example of the single-state low-resolution raw image. For the state-multiplexed FP scheme (Fig. 3.3(a2)), two adjacent LEDs are used for sample illumination, and thus, the corresponding raw image (Fig. 3.3(c1)) represents an incoherent summation of two coherent states (from two LEDs). The reconstructed high-resolution images for these two schemes are shown in Fig. 3.3(b2)-3.3(b3) and 3.3(c2-c3). Based on the state-mixed raw images, we also used the single-state FP scheme to reconstruct the high-resolution images in Fig. 3.3(d1)-3.3(d2) for comparison.

From Fig. 3.3, we can see that, the state-multiplexed FP is able to recover high-resolution sample images from state-mixed measurements, and the quality of the reconstructions is comparable to that of single-state FP. This experiment validates the effectiveness of the reported state-multiplexed FP recover routine.

### **3.4 Spectral multiplexing in Fourier ptychographic imaging**

One important application of the state-multiplexed FP scheme is multispectral imaging. Light sources with multiple wavelengths can be used to illuminate the sample from different incident angles, and the acquired images represent incoherent summations of the sample transmission profiles at different wavelengths. A state-multiplexed FP algorithm can then be used to reconstruct multiple high-resolution images at different wavelengths. In this section, we demonstrate such a state-multiplexed scheme for color multiplexing, which we will refer to as “color-multiplexed FP”. It is also important to acknowledge that, color multiplexing has recently been demonstrated for lensless ptychography by using the concept of translational diversity (laterally moving the sample over different spatial positions) [26].

The operation principle of color-multiplexed FP is shown in Fig. 3.4, where we used a color LED array for sample illumination and acquired low-resolution images using a monochromatic camera. Since R/G/B LED elements were turned on simultaneously in the acquisition process, the acquired images represent incoherent summations of sample profiles at R/G/B wavelengths. Such state-mixed raw data is then used to recover three high-resolution images at the corresponding wavelengths and produce a final color image of the sample.

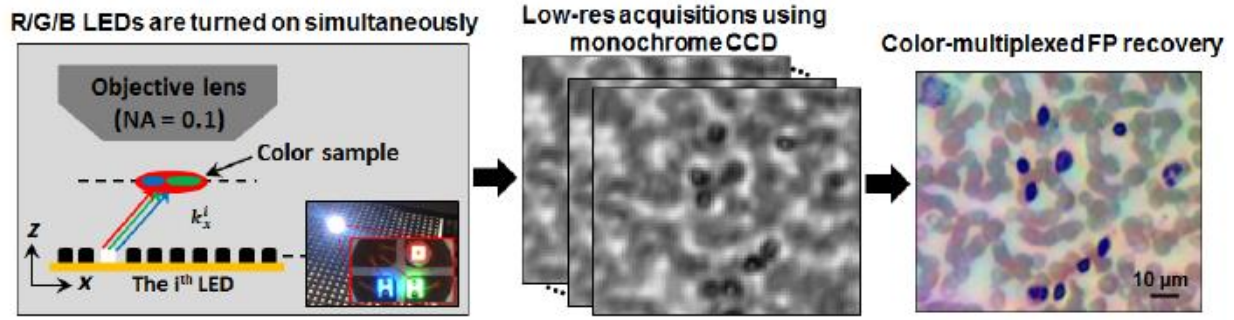


Fig. 3.4. Color-multiplexed FP scheme. R/G/B LEDs are turned on simultaneously for illumination. Low-resolution images are acquired using a 0.1 NA objective lens and a monochrome camera. A color-multiplexed FP recovery algorithm is then used to decouple the R/G/B channels from the low-resolution images. A high-resolution color image of the sample can be recovered using computation instead of spectral filters.

The recovery process of the color-multiplexed FP scheme is similar to that of state-multiplexed scheme. However, in this case, multiple sample estimates at different wavelengths are used in the workflow. As shown in Fig. 3.5, three sample estimates are used to generate the corresponding target images. The intensity components of the target images are summed up to generate the incoherent mixture  $I_t$ , and the target images are updated using the ratio between the actual measurement  $I_m$  and  $I_t$ . The updated target images are then used to modify the corresponding spectral regions of the sample estimates. The entire process is repeated for all intensity measurements, and iterated for several times until the solution converges. Lastly, the recovered images at different wavelengths are combined to produce a high-resolution color image.

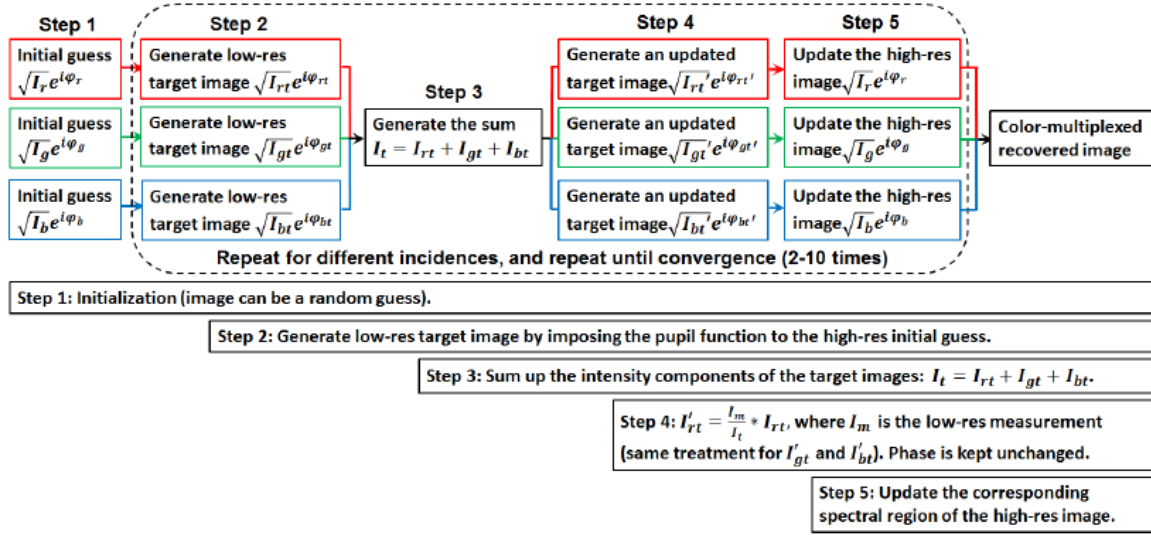


Fig. 3.5. Color-multiplexed FP recovery routine.

As before, we first validated the color-multiplexed FP using simulations. We simulated a  $15 \times 15$  color LED array with red/green/blue (632 nm, 532 nm, and 472 nm) elements lighting up simultaneously; other parameters being the same. The high-resolution input images (the ground truth) at three different channels are shown in Fig. 3.6(a1)-3.6(a3), and the corresponding color image is shown in Fig. 3.6(a4). The simulated low-resolution measurement is shown in Fig. 3.6(b), which represents an incoherent summation of three coherent states of the sample profiles. We then applied the color-multiplexed FP recovery algorithm to perform reconstruction, and the results are shown in Fig. 3.6(c1)-3.6(c4). We also quantified the image quality by calculating the mean-square errors, and the results are 0.5%, 0.4%, and 0.1% for Fig. 3.6(c1)-3.6(c3) respectively. We can see that, the color-multiplexed FP scheme is able to recover the color image of the sample from state-mixed measurements.



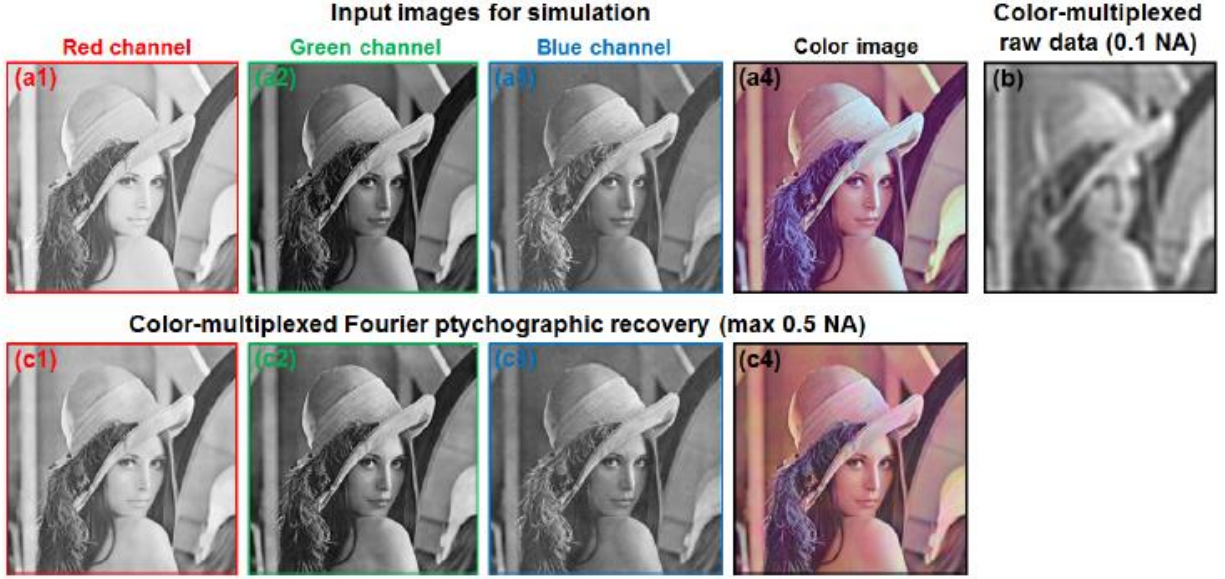


Fig. 3.6. Simulations of the color-multiplexed FP scheme. (a) Input R/G/B channels and the color image. (b) The low-resolution intensity measurement of the object, representing an incoherent summation of 3 object profiles at different wavelengths. (c) The color-multiplexed FP recovery (0.5 NA). The mean-square errors for (c1)–(c3) are 0.5%, 0.4%, and 0.1%, respectively.

We also validated the color-multiplexed FP scheme using a light microscope experiment, as shown in Fig. 3.7. We used a pathology slide (human breast cancer section, Carolina Inc.) as our sample, and R/G/B LEDs were turned on simultaneously for sample illumination. Low-resolution images were acquired using the 0.1 NA objective lens and the monochrome camera (parameters are the same as that for simulations). As such, these measurements represent incoherent mixtures of sample profiles at three wavelengths, as shown in Fig. 3.7(a). The color-multiplexed FP algorithm was then used to decouple into the R/G/B channels from the state-mixed measurements and recover the high-resolution color image of the sample. Figure 3.7(b1)–3.7(b3) demonstrate the recovered images for R/G/B channels, and the final color image is shown in Fig. 3.7(c). We also reconstruct the color image from three separated FP acquisitions (without state-mixing) in Fig. 3.7(d). As a comparison, the color image captured using a conventional 40X objective lens (0.6 NA) is shown in Fig. 3.7(e). However, we note that, the



focal plane of Fig. 3.7(e) may slightly shift when we switch the objective lens (the sample is about 15  $\mu\text{m}$  thick).

From this experiment, we can see that, the color-multiplexed FP algorithm is able to recover the high-resolution color image from the state-mixed measurements. We found that, the major noise source in our experiment was from the intensity uncertainty of the light source array. For example, the intensity fluctuations of R/G/B LED elements change the ratio of color components, creating state-decomposing errors and color mismatch problem for FP reconstructions. To address this problem, we can use a spectroscopic element to better calibrate the intensity values of the different LEDs in the array. Adaptive correction scheme can also be used to correct for intensity uncertainty in a post-processing manner [20]. We also found that, under the same illumination intensity, the intrinsic image contrast for the blue channel is weaker than that of red and green channels. To address this problem, we can adjust the illumination intensity ratio between different wavelength components. The optimal intensity ratio may depend on the employed staining technique. Nevertheless, the experiment shown in Fig. 3.7 provides a proof-of-concept demonstration of the color-multiplexed FP scheme.

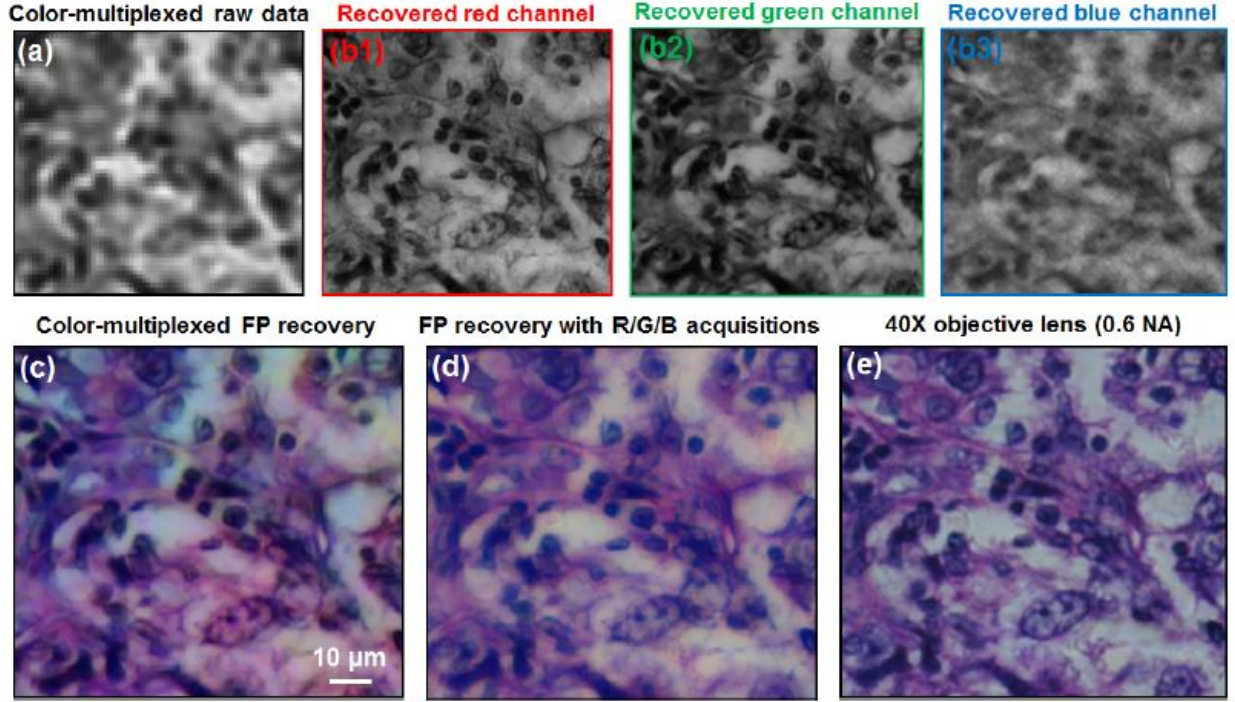


Fig. 3.7. Experimental demonstration of the color-multiplexed FP scheme. (a) Raw data of the color-multiplexed FP acquisition, representing incoherent summation of the sample profiles at three wavelengths. (b1)-(b3) The recovered color-multiplexed high-resolution images (0.5 NA) at red, green, and blue channels. (c) The recovered color image by combining (b1)-(b3) (with white balance). (d) The recovered color image (0.5 NA) using three separated FP acquisitions with individual red, green, and blue illumination (no state-mixing). (e) Color image using a conventional microscope with a 40X high-NA objective lens (0.6 NA).

### 3.5 Discussion and conclusion

In summary, we have developed and tested a state-multiplexed recovery scheme for Fourier ptychographic imaging. In this scheme, we use multiple target images for handling different coherent states of the light source and then update the high-resolution sample image accordingly. We have demonstrated the applications of the reported scheme for coherent-state decomposition and color-multiplexed imaging.

The state-multiplexed scheme can be used to model the partially coherent effects of the employed light sources. For example, the finite extent of the light source (related to spatial coherence) can be modeled as multiple point sources emitting light independently. The finite spectrum of the light source (related to temporal coherence) can be modeled as multiple light sources emitting light with different, but narrower passbands. The finite spatial extent or the

emission band of the LED can be separated into different point sources or narrower passbands until no difference between adjacent states can be detected. However, we note that, in our current implementation, the major reconstruction error comes from the intensity uncertainty of the LED array, not the partially coherent effects of the light source element. We also note that, instead of light up two components simultaneously, we can also light up more components in the array to form, for example, Hadamard basis patterns. By using the optimal basis, we may be able to reduce the number of acquisitions and raise the photon budget.

Furthermore, the spectrum-multiplexing scheme reported in this work can be used to replace thin-film interference filters, gratings or other optical components for spectral multiplexing and demultiplexing. We note that, the conventional ptychography approach typically requires the use of high-coherence light sources. The reported approach, on the other hand, considerably reduces the coherence requirement. In our demonstrations, we used a color LED array for imaging a pathology slide. It would be straight forward to extend the reported approach for more wavelengths using low-cost broadband LEDs.

Multispectral microscopy imaging is an emerging modality for various biomedical applications. This technology uses visible light as well as ultraviolet and infrared light to acquire more information from specimens. With the rich information of the 3D multispectral data cube, tissue constituents can be more easily identified with their spectral signatures [28]. For example, multispectral microscopy has been demonstrated for differentiating prostate cancer [29], cancerous colon biopsies [30], and melanoma [31] using pathology slides. It has also found applications in chemical imaging and sensing using functionalized nanoparticles [32]. Different from other multispectral imaging geometries, the reported FP scheme can be implemented with most existing microscopes in a cost-effective manner. The resolution and throughput are also adequate

for microscopy screening. We anticipate that, the reported scheme can provide a practical solution for multispectral microscopy and open up exciting opportunities for computational multispectral imaging in the near future. Our on-going efforts include the development of a high-power white light LED array for sample illumination.

Finally, we note that, the effectiveness of the spectrum-multiplexed approach may depend on the data redundancy and the compressibility of the sample image [20]. This relationship can be directed to the recent development of compressive sensing [21, 33–35]. Further investigations along this line are highly desired.

## Chapter 4

### High-resolution fluorescence imaging via pattern-illuminated Fourier ptychography (Adapted from [77])

#### 4.1 introduction and background

The lateral resolution of conventional fluorescence microscopy is determined by the diffraction limit of the employed optics:  $\lambda/(2\text{NA}_{\text{obj}})$ , where  $\lambda$  is the wavelength of the incidence and  $\text{NA}_{\text{obj}}$  is the numerical aperture (NA) of the objective lens [1]. This diffraction limit, however, is established under the assumptions of single image acquisition and uniform light illumination. It is possible to combine multiple acquisitions with non-uniform illuminations to bypass this resolution barrier. Frequency mixing between the sample and the non-uniform illumination pattern shifts the high-frequency components to the passband of the collection optics. Therefore, the recorded image contains sample information that is beyond the diffraction limit. Structured illumination microscopy (SIM) is one good example towards this end [36–44]. A typical SIM setup projects a sinusoidal pattern at the sample plane and uses at least three phase steps to laterally shift the pattern across the sample. The corresponding images will be used to improve the resolution along the orthogonal direction of the sinusoidal pattern. Following a similar logic, sinusoidal patterns with other orientations will be used to improve the resolution along other directions. In the linear regime, the SIM approach is able to improve the diffraction-limited resolution by a factor of two, and thus, the final achievable

NA can be twice of the objective's NA. The capability of bypassing diffraction limit has made SIM a popular tool for super-resolution fluorescent imaging. In this chapter, we report a novel fluorescence imaging approach, termed pattern-illuminated Fourier ptychography (FP), for bypassing the diffraction limit of the employed optics. Similar to SIM and other speckle

illumination schemes [36–55], the reported approach uses non-uniform intensity patterns for sample illumination and acquires the corresponding diffraction-limited intensity images. Based on the acquired images, a novel Fourier ptychographic recovery algorithm is used to reconstruct the high-resolution sample image in an iterative manner. The recovery process starts with a low-resolution intensity image as the initial guess. This initial guess is then sequentially updated by other low-resolution measurements taken under different illumination patterns. Similar to the original FP approach [57–63], the iterative updating process also switches between the spatial and Fourier domains. In the spatial domain, we use the pattern-illuminated low-resolution images as intensity constraints for the sample estimate. In the Fourier domain, we use the incoherent optical transfer-function of the objective lens as the object support constraint for the solution. This sequential updating process is iterated until the sample estimate converges (5-20 times).

We note that, the strategy of using non-uniform illumination for improving lateral or axial resolution is not new [36–44]. However, the use of the FP framework [2, 3, 16, 20, 57-58] to recover a high-resolution fluorescence image is new and may provide an alternative solution to existing SIM and speckle illuminating platforms. As the use of fluorescence microscopy is prolific in modern biological research and clinical diagnosis [2, 3, 16, 20, 57-58], the reported approach may open up new opportunities for the Fourier ptychographic imaging paradigm.

#### **4.2 Pattern-illuminated Fourier ptychography**

As a coherent imaging technique, the original FP approach cannot be used for fluorescence microscopy. The reason is very simple: fluorophores are not responsive to phase variation of the excitation waves. In the original FP prototype, no matter which angle we illuminate the sample, the fluorescence emission remains unchanged and no additional information can be extracted from the raw images. To modify the FP recovery concept for

fluorescence microscopy, we can simply replace the plane wave illuminations with intensity-varied patterns. In this case, fluorophores are responsive to the intensity variations, and each low-resolution image provides additional information for the high-resolution sample profile. We term such a scheme as pattern-illuminated Fourier ptychography.

As shown in Fig. 4.1, the pattern-illuminated FP approach uses multiple intensity-varied pattern  $P_n$  ( $n = 1, 2, 3, \dots$ ) to illuminate the object  $I_{obj}$  and acquires the corresponding low-resolution images  $I_n$  ( $n = 1, 2, 3, \dots$ ) through the objective lens. The proposed algorithm aims to recover the high-resolution object image  $I_{obj}$  from the low-resolution images  $I_n$  ( $n = 1, 2, 3, \dots$ ). Here we assume that the illumination pattern  $P_n$  is known. Later in this section, we will extend the recovery framework for an unknown illumination pattern.



Fig. 4.1. Overview of the pattern-illuminated FP recovery scheme. Multiple pattern-illuminated low-resolution images  $I_n$  ( $n = 1, 2, 3, \dots$ ) are used to recover the high-resolution sample image  $I_{obj}$ . In the last low-resolution image  $I_n$ , the high-frequency illumination pattern is filtered out by the low-NA objective lens.

The image formation process can be expressed in the Fourier space as follow

$$\mathcal{F}(I_n) = OTF \cdot \mathcal{F}(I_{obj} \cdot P_n), \quad (1)$$

where  $\mathcal{F}()$  denotes the Fourier transform of the image, and  $OTF$  denotes the incoherent optical-transfer-function of the objective lens. There are two multiplication steps in Eq. (1): one in the spatial domain and one in the Fourier domain. In the spatial domain, the object emission profile is multiplied with the illumination pattern to produce a target image  $I_{tn}$ :  $I_{tn} = I_{obj} \cdot P_n$ . In the Fourier domain, the incoherent OTF is multiplied with the spectrum of the target image to produce the

spectrum of the measurement:  $\mathcal{F}(I_n) = OTF \cdot \mathcal{F}(I_{obj} \cdot P_n)$ . To recover the high-resolution object emission profile  $I_{obj}$ , we need to invert these two multiplication steps in both the spatial and Fourier domain.

The flow chart of the recovery algorithm is shown in Fig. 4.2. Briefly speaking, it starts with an initial guess of the sample emission profile (step 1). This initial guess is then sequentially updated by other low-resolution measurements taken under different illumination patterns (step 2). The updating process is iterated until the solution converges (step 3).

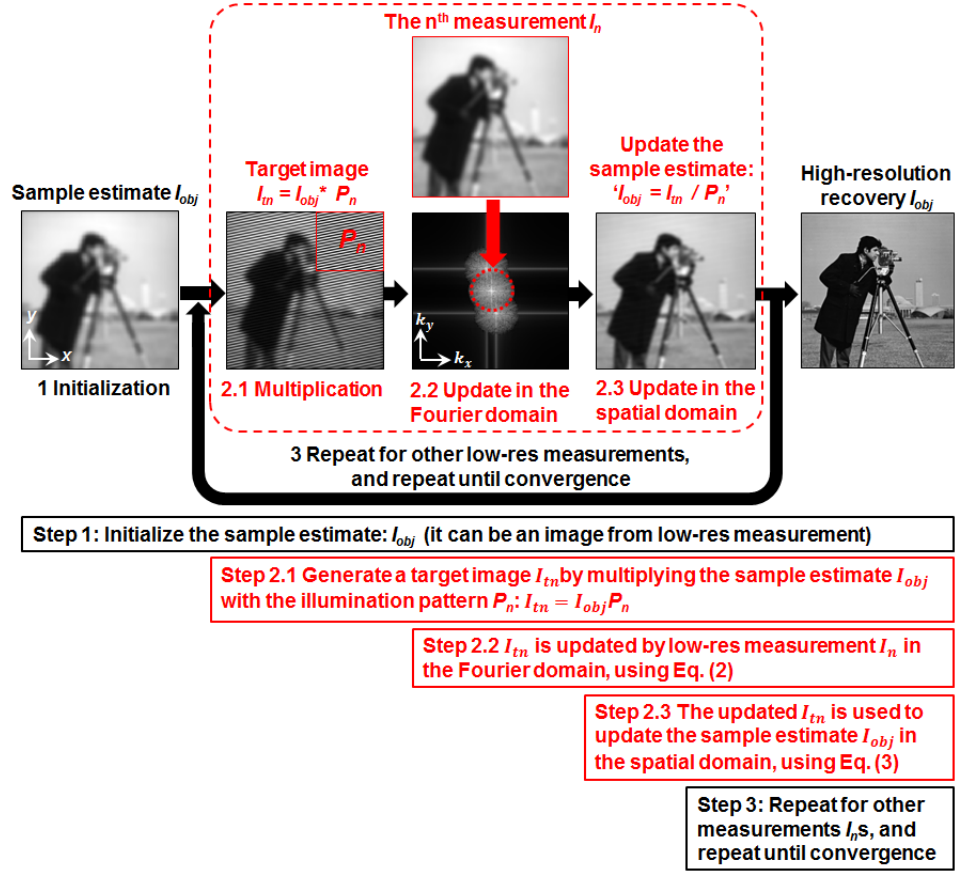


Fig. 4.2. Flow chart of the pattern-illuminated FP algorithm.

These three steps can be explained in details as follow. Step 1: it starts with an initial guess of the sample emission profile  $I_{obj}$ . This initial guess can be an interpolation of one low-resolution measurement; it can also be a random guess. Step 2.1: the initial guess is then multiplied with the



illumination pattern  $P_n$  to produce a target image  $I_{tn}$  in the spatial domain:  $I_{tn} = I_{obj} \cdot P_n$ . Step 2.2: the target image  $I_{tn}$  is updated by the low-resolution measurement  $I_n$  in the Fourier space as follow

$$\mathcal{F}(I_{tn})^{updated} = \mathcal{F}(I_{tn}) + OTF \cdot (\mathcal{F}(I_n) - OTF \cdot \mathcal{F}(I_{tn})) \quad (2)$$

The term  $\mathcal{F}(I_{tn})^{updated}$  is then transformed back to the spatial domain to produce an updated target image  $I_{tn}^{updated}$ . Step 2.3: the updated target image  $I_{tn}^{updated}$  is then used to update the high resolution sample estimate in the spatial domain using the following equation

$$I_{obj}^{updated} = I_{obj} + \frac{P_n}{(\max(P_n))^2} \cdot (I_{tn}^{updated} - I_{obj} \cdot P_n) \quad (3)$$

Step 3: The updating process is repeated for all different illumination patterns and iterated until the solution converges. The convergence metric is the mean-square-error (MSE) of two consecutive recovered solutions. The process stops if the MSE is smaller than a pre-defined value.

We note that, Eq. (2) is performed in the Fourier domain and Eq. (3) is performed in the spatial domain. Similar procedures can also be found in the pupil recover scheme of the original FP approach [59], as well as in the conventional ptychography approach [60, 61]. In conventional SIM settings, the illumination patterns are generated by two beam interference, and thus, the patterns are known. In this case, Eq. (2)-(3) can be used to recover the high-resolution sample image. We note that, different from the conventional SIM recovery scheme, the reported algorithm requires no phase stepping of the sinusoidal pattern.

It is straight forward to extend the reported framework for handling unknown pattern. In this case, one unknown pattern can be translated to different spatial positions or rotated with different orientations. At each position, one low-resolution image is acquired using the low-NA objective

lens. Similar to the recovering process of the sample image  $I_{obj}$ , we can assign an initial guess for the unknown pattern  $P_{unknown}$ . In our implementation, we use uniform illumination (i.e.,  $P_{unknown}=1$ ) as the initial guess. To recover this unknown pattern, we only need to add one sub-step, step 2.4, in the image updating process. In this sub-step, the updated target image  $I_{tn}^{updated}$  is used to update the unknown pattern as follow:

$$P_{unknown}^{updated} = P_{unknown} + \frac{I_{obj}}{\max(I_{obj})} \cdot (I_{tn}^{updated} - I_{obj} \cdot P_{unknown}(x - x_n)) \quad , \quad (4)$$

where  $x_n$  is the scanning positions of the sample.

We note that, the use of translated illumination pattern has been demonstrated by Ventalon and Mertz for improving the axial resolution of fluorescence microscopy [22]. Our work, on the other hand, uses the translated illumination pattern to improve the lateral resolution of the sample emission profile. Furthermore, the reported recovery algorithm does not rely on the statistical nature of the illumination patterns. The iterative algorithm is able to recover both the high-resolution sample image and the unknown pattern at the same time.

### 4.3 Simulations of the pattern-illuminated FP framework

We first simulated the use of the reported framework for conventional SIM settings, where the known sinusoidal patterns are used for sample illumination. Fig. 4.3(a1) shows the simulated raw image acquired by a 0.15 NA objective lens (0.25  $\mu\text{m}$  pixel size). Fig. 4.3(a2) shows the same raw image with 1% additive Gaussian noise. Fig. 4.3(a3) shows the corresponding Fourier spectrum of the raw image.

Next, we used different number of sinusoidal patterns for sample illumination and perform image recovery using the pattern-illuminated FP algorithm. In Fig. 4.3(b), we use 18 sinusoidal patterns for illumination. We only changed the orientations of the sinusoidal patterns and no phase

stepping is needed. The frequency of the sinusoidal patterns corresponds to an illumination NA of 0.1, and thus, the NA of the final recovered image in Fig. 4.3(b) is 0.25. In Fig. 4.3(c), we use 36 sinusoidal patterns with two different frequencies. The frequency of the first 18 patterns corresponds to an illumination NA of 0.1, and the frequency of the other 18 patterns corresponds to an illumination NA of 0.25. Therefore, the NA of the final recovered image shown in Fig. 4.3(c) is 0.4. Following a similar logic, we use 54 sinusoidal patterns in Fig. 4.3(d), corresponding to three different illumination NAs (0.1, 0.25, and 0.4). The NA of the final recovered image shown in Fig. 4.3(d) is, therefore, 0.55.

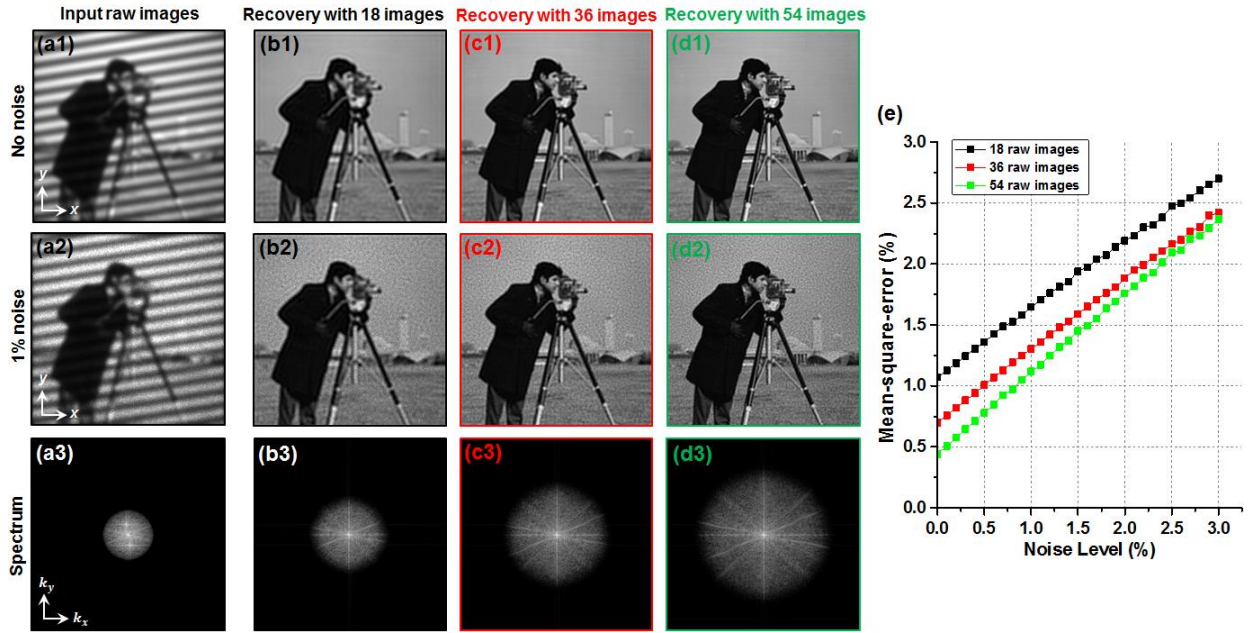


Fig. 4.3 Pattern-illuminated FP recovery using sinusoidal patterns. (a1) Simulated raw image without noise, and (a2) with 1% additive noise. (a3) The Fourier spectrum of (a1). FP recoveries using (b) 18 raw images, (c) 36 images, and (d) 54 images. We used 15 loops for the FP reconstructions. For the noise-free cases, the corresponding MSEs are 1.07%, 0.70%, and 0.44% for (b1)-(d1). For the cases with 1% noise, the corresponding MSEs are 1.65%, 1.30%, and 1.12% for (b2)-(d2). (e) The MSE is plotted as function of different noise levels. Different color lines correspond to different number of raw images.

We also study the noise performance of the proposed algorithm by adding different amounts of Gaussian noise to the raw image. Fig. 4.3(b2)-4.3(d2) demonstrate the recovered images with 1% additive noise. Fig. 4.3(e) shows the MSE as a function of different noise levels. We can see

that, the image quality degrades linearly as a function of the additive noise. Therefore, the reported framework is robust to the additive noise.

In a practical experiment, it is difficult to precisely characterize the illumination pattern. Therefore, it is important to extend the reported FP framework for handling unknown illumination patterns. As we have discussed in the section 2, we can use one unknown pattern in our framework and translate this pattern into different spatial positions for sample illumination. The object and the unknown pattern can be updated using Eq. (3) and Eq. (4) in the iterative recovery process.

In Fig. 4.4, we simulated the case of translating one unknown speckle pattern to 169 different spatial positions for sample illumination. The simulated raw images are shown in Fig. 4.4(b). The recovered unknown illumination pattern and object image are shown in Fig. 4.4(c) and 4.4(d). The MSE of Fig. 4.4(d1) is 0.4%, comparable to the case of Fig. 4.3(d1). We note that, the unknown speckle pattern in this simulation is fully randomized. Therefore, the upper frequency limit of the pattern shown in Fig. 4.4(a) is only determined by the employed pixel size. In a practical experimental setting, the upper frequency limit for the speckle pattern is, however, determined by the employed optics. For example, if a 0.9 NA condenser is used to focus the speckle pattern onto the sample, the maximum NA of the speckle pattern is 0.9. The corresponding frequency support can then be imposed for illumination pattern at each iteration loop (the components outside the frequency support are set to zero).

The simulations shown in Fig. 4.3 and Fig. 4.4 validate the working principle of the reported pattern-illuminated FP recovery algorithm.

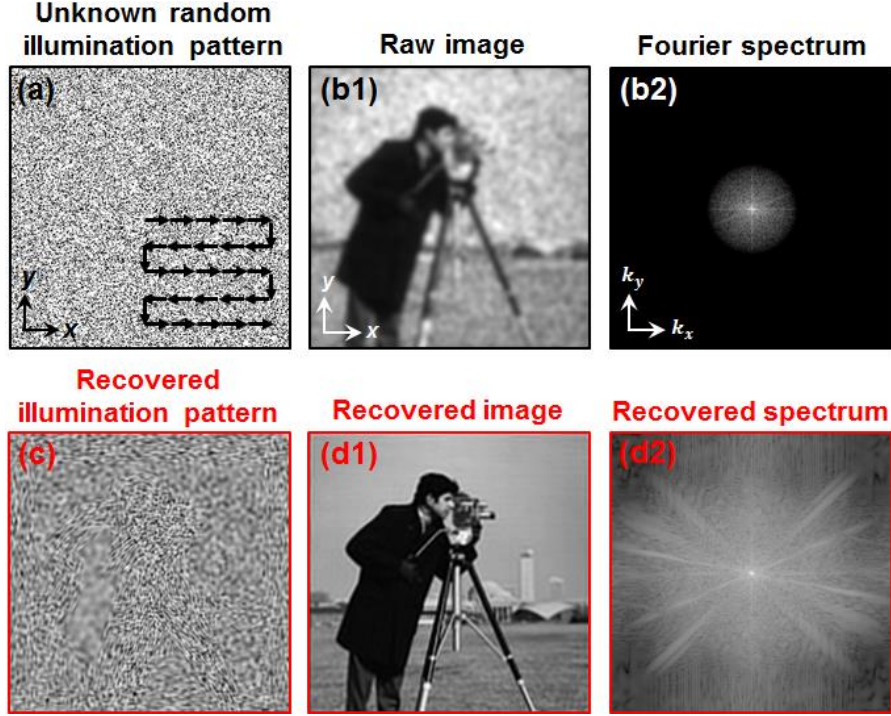


Fig. 4.4 Pattern-illuminated FP recovery using unknown patterns. (a) The unknown illumination pattern (random pattern) is translated into 169 different spatial positions. (b1) The simulated raw image. (b2) The Fourier spectrum of (b1). (c) The recovered illumination pattern. (d) The recovered high-resolution object image and its Fourier spectrum. We used 15 loops for the FP reconstructions. The MSE of (d1) is 0.4%.

#### 4.4 Experimental demonstration of the pattern-illuminated FP approach

In this section, we will use the reported framework to improve the resolution of a commercially available fluorescence microscope (Nikon Ti-E motorized microscope). The experimental setup is shown in Fig. 4.5, where a 488 nm laser diode is used as the light source and a diffuser is inserted into the epi-illumination arm. The excitation light, thus, forms a random speckle pattern on the sample. The resulting fluorescence emission then passes through the detection path and reaches the CCD sensor. To acquire a pattern-illuminated FP dataset, we only need to move the sample to different spatial positions using the motorized stage and acquire the corresponding fluorescence images. We note that, our setup is compatible with most existing epi-illuminated microscope platforms; no major hardware modification is needed.

In our demonstration, we used a mouse kidney section (Molecular Probes F24630, Life Technology) as our sample. The central wavelength of the mission filter is 525 nm, with a 50 nm bandwidth (Semrock FF03-525/50-25). We use a 10X 0.25 NA objective lens (Nikon) and a CCD camera (Andor Clara Interline CCD) for image acquisition. The sample is moved to 49 different positions in our experiment, and the acquired images are used to recover both the high-resolution sample emission profile and the unknown illumination pattern. Fig.4.5 (b1)-(b4) demonstrate 4 out of 49 acquired raw images using the reported platform. As expected, we can clearly see the speckle-like features from these raw images. We note that, the 10X, 0.25 NA objective lens is used both for illumination and light collection in the reported setting. Therefore, the upper frequency limit of the speckle pattern is determined by the incoherent optical-transfer-function of the 0.25 NA lens. In the recovery process, we imposed the corresponding frequency support to constraint the illumination pattern at each iteration loop.

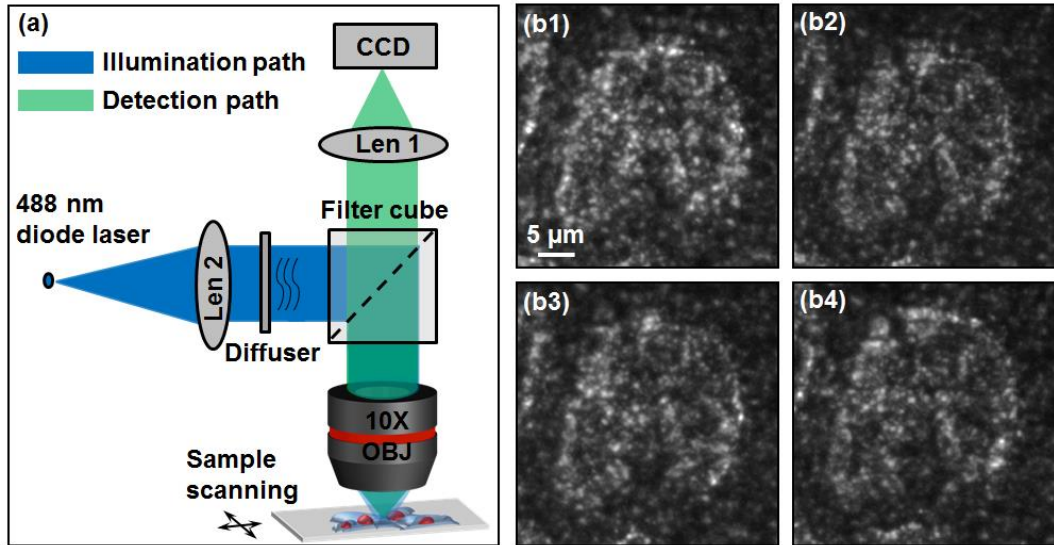


Fig. 4.5 (a) Pattern-illuminated FP setup. A diffuser is placed at the epi-illuminated arm of the microscope platform. The excitation light from the objective lens forms a speckle pattern on the sample. The resulting fluorescence emission from sample is then collected by the objective lens and detected by the CCD camera. (b1)-(b4) 4 acquired raw images.

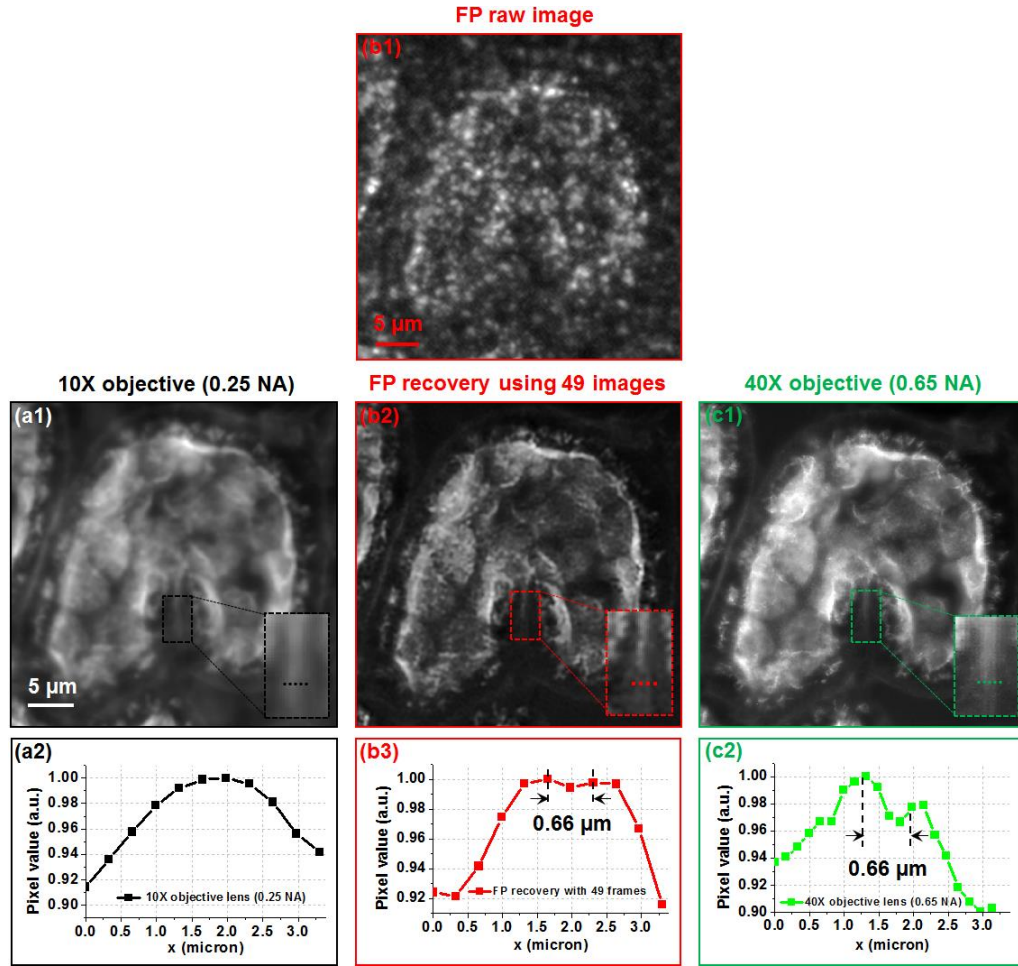


Fig. 4.6 Imaging performance of the pattern-illuminated FP approach. (a1) Sample image acquired using the 10X objective lens with uniform illumination. (b1) Speckle-illuminated raw image. (b2) FP recovery using 49 raw images. (c1) Sample image acquired using a 40X high-NA objective lens. (a2), (b3), (c2) Intensity lines traces of the highlighted features in (a1), (b2), (c1). For (a1) and (c1), we averaged multiple frames to get a similar photon budget as (b2).



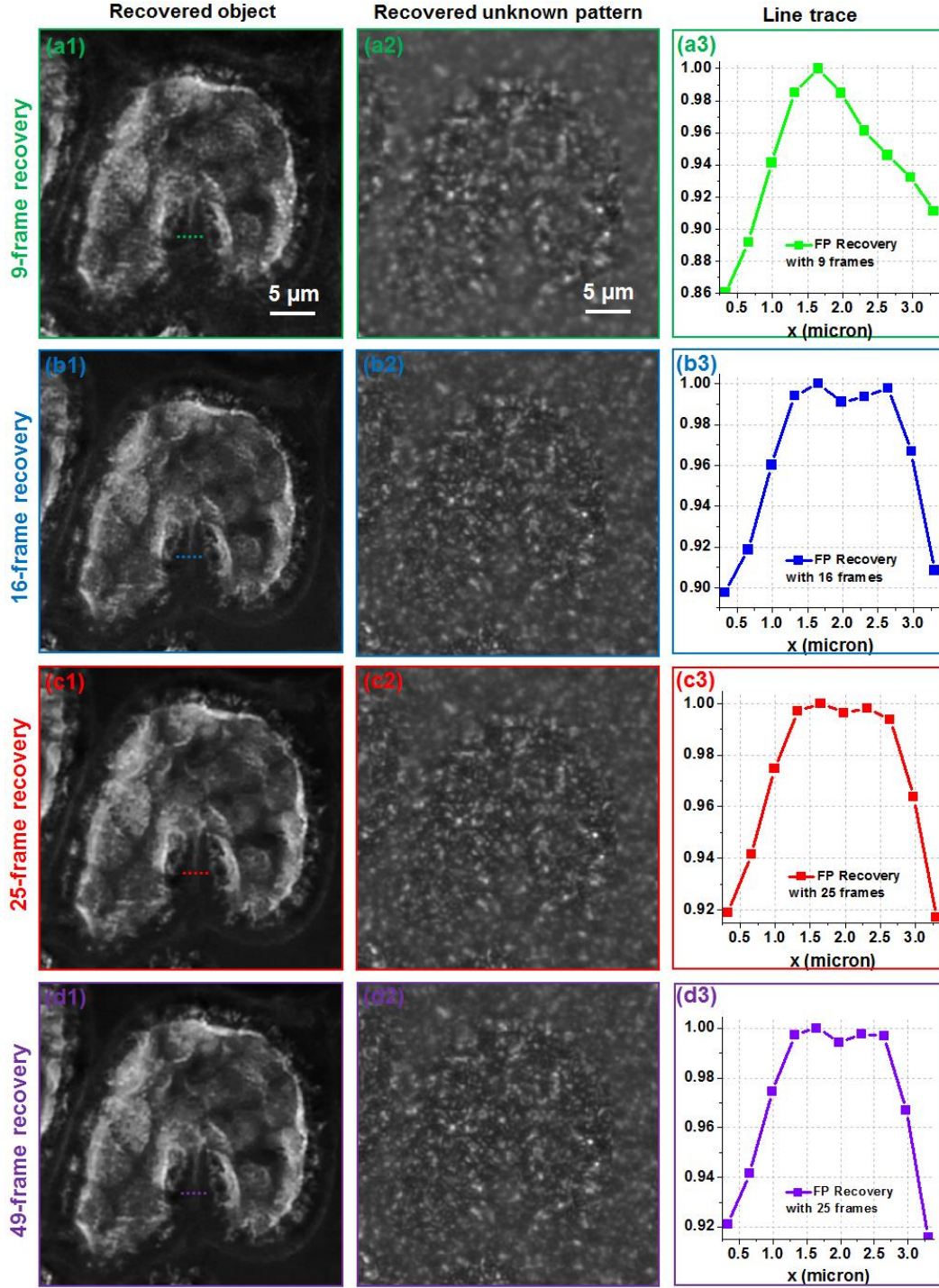


Fig. 4.7. FP reconstructions using different number of raw images. We used 5-9 loops for the iterative recovery process. (a) 9-frame recovery. (b) 16-frame recovery. (c) 25-frame recovery. (d) 49-frame recovery. (a1)-(d1) The recovered object profiles. (a2)-(d2) The recovered unknown illumination patterns. (a3)-(d3) Intensity lines traces corresponding to the highlighted features in (a1)-(d1). The FP reconstruction converges with 25 raw images.

Fig. 4.6 demonstrates the performance of the pattern-illuminated FP approach. For Fig. 4.6(a), we use the same 10X objective lens with uniform illumination to capture the sample image. Fig.



4.6(b1) shows the raw FP image under the speckle illumination. Fig. 4.6(b2) shows the FP reconstruction using 49 raw images. Fig. 4.6(c1) shows the image captured by a 40X high-NA objective lens. Fig. 4.6(a2), 4.6(b3), and 4.6(c2) show the intensity line traces of a small feature of the sample, corresponding to the highlighted regions of Fig. 4.6(a1), 4.6(b2) and 4.6(c1). As shown in Fig. 4.6(a2), we cannot resolve the two lines using the 10X objective lens. We can, however, barely resolve the two-line feature using the FP recovered image in Fig. 4.6(b2). We also observe the same feature from the image captured by the 40X high-NA objective lens in Fig. 4.6(c). Therefore, from the comparison of this set of images, we verify that the observed two-line feature is not an artifact of the FP reconstruction process. From Fig. 4.6(b) and 4.6(c), the distance between these two lines is estimated to be  $0.66\text{ }\mu\text{m}$ . By Rayleigh criteria, the NA of the FP recovered image is, thus, determined to be 0.47. The corresponding resolution enhancement factor is  $\sim 1.8$ , close to the theoretical limit of 2.

We further compare the FP reconstructions using different number of raw images in Fig. 4.7. Fig. 4.7(a)-4.7(d) show FP reconstructions using 9 frames, 16 frames, 25 frames, and 49 frames respectively. From this comparison, we can see that, the FP reconstruction converges with 25 raw images.

## Chapter 5

### **Field-portable high-resolution microscope using a cellphone lens (Adapted from [76])**

#### **5.1 Introduction and background**

Optical microscopy pervades almost all aspects of modern bioscience and clinical applications. A typical microscope consists of an objective lens, space for relaying the image, and a tube lens to project a magnified image onto the eyepiece or a camera. To achieve high-resolution microscopic imaging, a precise and expensive objective lens is needed for collecting light over a large angle. The challenge for miniaturizing the conventional microscope platform comes from intrinsic aberrations of the lens elements. The perfect lens obeying ray diagrams does not exist in the physical world. A microscope objective particularly highlights the lens aberrations due to the large collection angle of the entrance pupil. To improve the performance of a standard microscope, we need to pack in more lens elements to correct for both chromatic and monochromatic aberrations.

In recent years, there has been increasing interest in developing portable microscope platforms that would benefit remote clinics or be used in resource-limited environments [62-67]. Lensless microscopy is a good example of this direction. It has been shown that, sub-micron resolution can be achieved using various lensless imaging techniques, such as optofluidic microscopy [62, 64], digital in-line holography [64, 67, 68], and contact imaging microscopy [66]. Applications of these techniques range from malaria parasite screening and single cell tracking, to real-time cell culture monitoring and etc. While these techniques have been successfully demonstrated, they are limited to a small range of samples. Optofluidic microscopy requires the sample to flow across a microfluidic channel. It works well for dispersible samples such as blood, fluid cell cultures, and other suspensions of cells or organisms, but is incompatible with adherent samples or samples on

glass slides. Digital in-line holographic microscopy records interference intensity distribution of a target under coherent light illumination. Reconstruction algorithms then recover the complex transmission profile of the sample. This approach works well for sparse sample such as well-isolated blood smear slides but the algorithms cannot handle confluent samples such as pathology slides. The reason for this limitation is the well-known loss of phase information during the intensity recording process. In order to recover the complex sample transmission profile, confined object constraints (sparsity constraints) need to be imposed in the spatial domain. The contact imaging approach requires the sample placed at close proximity to the sensing surface and, thus, cannot handle conventional microscope glass slides. While techniques for mitigating these limitations have been reported [68, 69], the image quality is generally not as good as a conventional microscope.

Here we report our effort on the development of a portable high-resolution microscope platform, termed FPscope, using the Fourier ptychography (FP) approach [2, 3]. FP is a recently developed computational imaging procedure that synthesizes a number of variably illuminated, low-resolution intensity images in Fourier space to produce a high-resolution complex sample image. The FP imaging procedure transforms the general challenge of optical design that is coupled to the physical limitations of the system's aberrations to one that is solvable by computation. The final achievable resolution of FP is determined by the largest incident angle of the illumination beam, not the numerical aperture (NA) of the objective lens. The recovery information using FP is shown to be quantitative in nature. Optical aberration can also be digitally corrected by introducing a complex pupil function in the recovery process [70, 71]. Recently, we have also extended the FP procedure to multispectral imaging [58], 3D holographic imaging [72], and super-resolution macroscopic imaging beyond the diffraction limit [72].

## 5.2 System design of the FPscope

The core component of the FPscope is a cellphone lens. The large consumer market has made cellphone lens modules available at low-cost and in high-quality. For a conventional cellphone camera, the lens module is used to demagnify the scene onto the image plane of the camera, where the image sensor is located. In the FPscope, we use the cellphone lens module (Nokia 808) in the reverse manner; we replace the image sensor with sample specimen and use the cellphone lens to project the magnified image onto a low-cost CCD camera (DMM 31AU03, The Imaging Source). The magnification factor can be tuned by adjusting the distance between the sample and the cellphone lens. In our design, the magnification factor was chosen to be 4.5, to satisfy the Nyquist sampling requirement. We note that the configuration shown in Fig. 5.1(a) is not new. We have demonstrated the same configuration (using a lens in the reverse manner and projecting the magnified image onto the detector) for gigapixel imaging [73]. However, the use of a cellphone lens in conjugation with the FP algorithm enables a cost-effective solution for field-portable microscopy imaging.

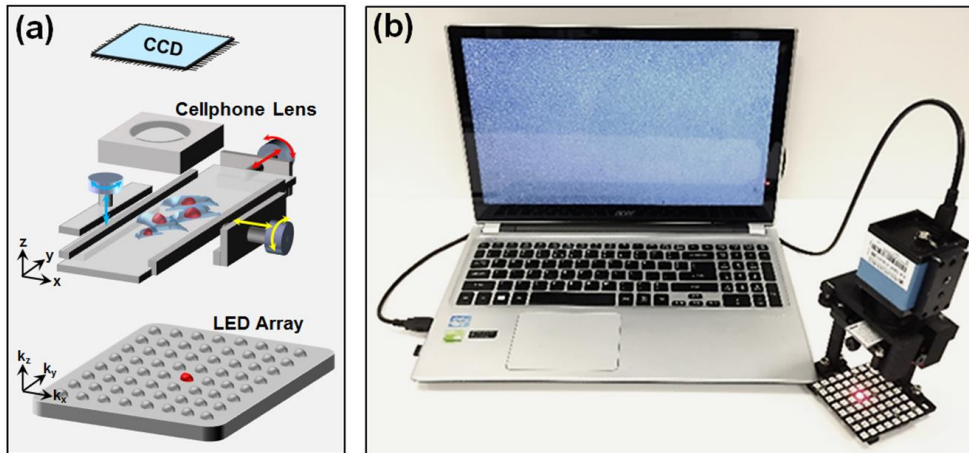


Fig. 5.1 System design of FPscope. (a) A cellphone lens is used in a reverse manner. The magnified sample image is projected onto a CCD sensor. An 8 by 8 LED matrix is used for sample illumination. (b) The assembled FPscope connected to a computer.

To supersede the diffraction limit of the lens module, we used an 8 by 8 LED array for sample illumination. Each LED element of the array illuminates the sample from an oblique incident

angle, and the corresponding image is acquired using the cellphone lens with a 0.15 NA. The acquired 64 images are then synthesized in Fourier space using the Fourier ptychographic algorithm. The final synthetic NA is determined by the largest incident angle of LED illumination, and it can be adjusted by changing the distance between the LED array and the sample. In our design, the distance between the LED array and the sample is chosen to be  $\sim 10$  cm, corresponding to a maximum synthetic NA of 0.5. We also note that if the illumination is placed too close to the sample, there won't be enough Fourier spectrum overlap between two adjacent LEDs [74].

We designed a 3D manual stage to move the sample in the x-y plane and to adjust the focal position. Most of the components in our design were produced using a Makerbot 3D printer. The components were assembled with springs and screws. Fig. 5.1(b) shows the FPscope connected to a computer.

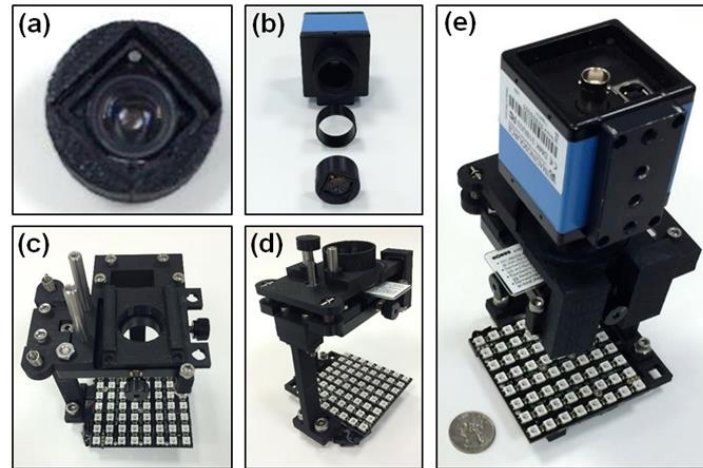


Fig. 5.2 The assembling process of the FPscope. (a) A Nokia cellphone lens is fit in to a plastic case. (b) The case is assembled onto a CCD camera. (c) The assembling of the x-y stage and the slide holder. (d) The assembling of the z stage. (e) The final assembled FPscope.

Fig. 5.2 shows the assembly process of the FPscope. Fig. 5.2(a) and (b) show the cellphone lens mount in front of the CCD camera. Fig. 5.2(c) shows the x-y stage and the slide holder assembly. Fig. 5.2(d) shows the z stage assembly. The final assembled FPscope is shown in Fig.

5.2(e). The dimensions of the FPscope are 8 x 8 x 16 cm. The mass of the platform is about 250 grams, mostly of which is from the CCD camera.

### 5.3 System characterization of the FPscope

We characterized the system resolution performance by imaging a USAF target. In this experiment, we captured 64 low-resolution images and used them to recover a high-resolution image using the FP algorithm. The recovery process switches between the spatial and Fourier domains. In the spatial domain, the acquired low-resolution images are used to constrain the amplitude of the solution. In the Fourier domain, the coherent transfer function (i.e., the pupil function) of the cellphone lens is used as a support constraint for the solution. This support constraint is digitally panned across Fourier space to reflect the angle-varied illuminations of the 8 by 8 LED array. The detailed recovery procedure can be found in [2, 3].

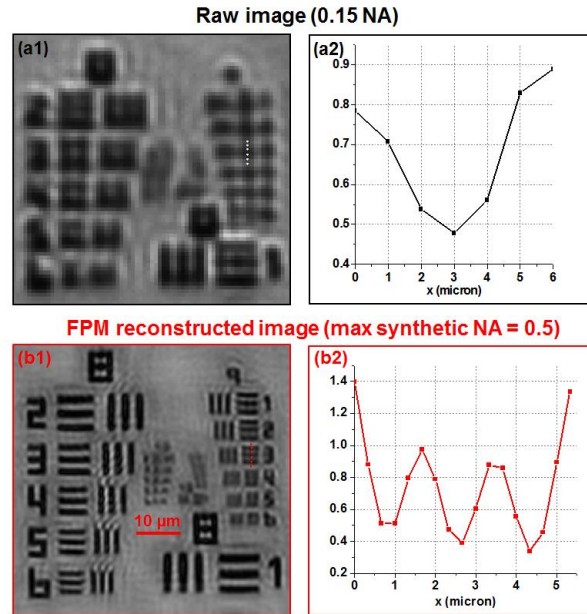


Fig. 5.3 Resolution characterization of the FPscope. (a) One of the 64 low-resolution raw images captured using the cellphone lens. (b) The FP recovered image, where feature of group 9, element 3 can be clearly resolved.

Fig. 5.3(a) shows the raw image captured by the cellphone lens; the NA was measured to be ~0.15. Fig. 5.3(b) shows the recovered image, and the maximum synthetic NA was, as expected,

about 0.5. We can clearly resolve the feature in group 9, element 3, where line-width is  $0.78\ \mu\text{m}$ . Another advantage of the FPscope is the ability to incorporate pupil correction in the recovery process. By introducing a second-order defocused pupil function, we can digitally tune the focal position along the optical axis. Fig. 5.4 demonstrates the digital refocusing capability of the FPscope. We can see that, the depth-of-focus of the FPscope is longer than 0.1 mm without trading off resolution. This much depth-of-focus is orders of magnitude longer than that of conventional microscope objective lens with a similar NA. Therefore, the FPscope is significantly less prone to sample misalignment.

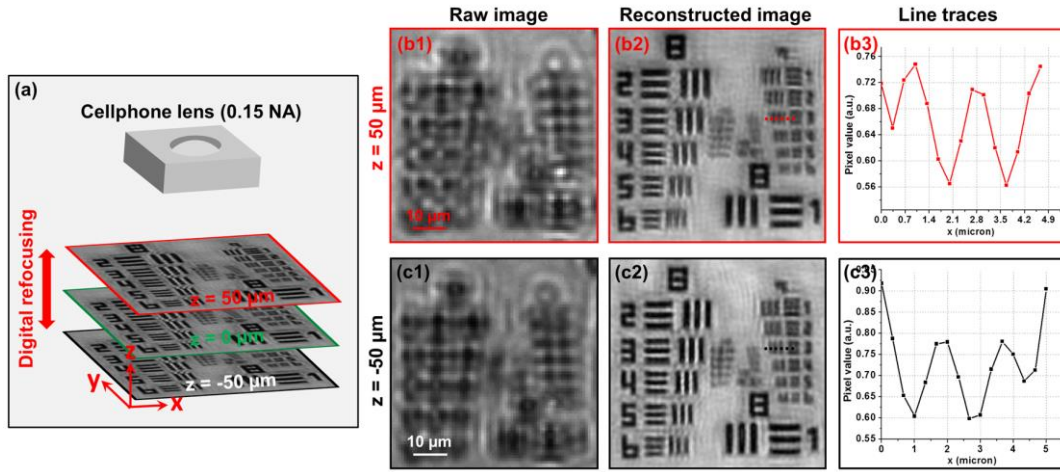


Fig. 5.4 (a) Depth-of-focus characterization of the FPscope. One of the low-resolution raw images captured at (b1)  $z = 50\ \mu\text{m}$  and (c1)  $z = -50\ \mu\text{m}$ . (b2-b3), (c2-c3) The FP reconstructions by introducing a second-order defocused pupil function at the recovery process. The depth-of-focus is orders of magnitude longer than that of conventional microscope objective lens with similar NA.

#### 5.4. Demonstration of the FPscope with biological samples

We also used the FPscope to image biological samples. In the first experiment, we used a blood smear as our sample. Fig. 5.5(a) shows the low-resolution raw image of the blood smear. Fig. 5.5(b)-(c) show the recovered intensity, phase images of the sample. We also recovered the high-resolution color image of the sample by combining the FP constructions from R/G/B illuminations.

Fig. 5.5(e) shows the image captured using a conventional microscope with a 40X, 0.75 NA objective lens.

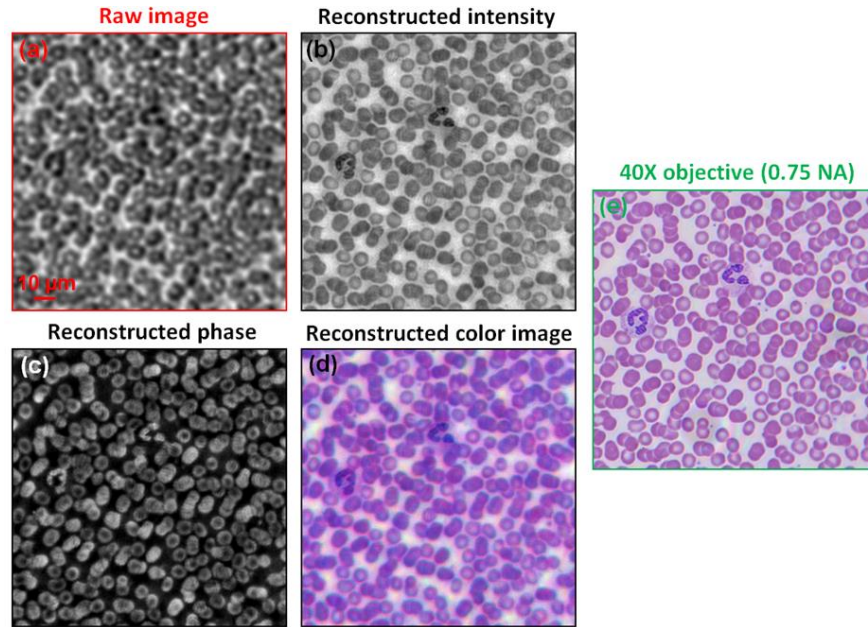


Fig. 5.5 (a) Raw image of a blood smear (0.15 NA). FP recovered intensity image (b), phase (c), and color image (d). The maximum synthetic NA is 0.5. (e) The image captured using a conventional microscope with a 40X, 0.75 NA objective lens.

In the second experiment, we used a pathology slide as our sample (human adenocarcinoma of breast section, Carolina), as shown in Fig. 5.6. The full field-of-view is about 1.2 mm by 0.9 mm and corresponding computational time is about 50 seconds in MATLAB using a personal computer with an i7 CPU. High-resolution views are provided for two regions, one at the central field-of-view, and the other one at the edge. Images captured with a conventional microscope with a 0.75 NA objective lens are also provided for comparison.



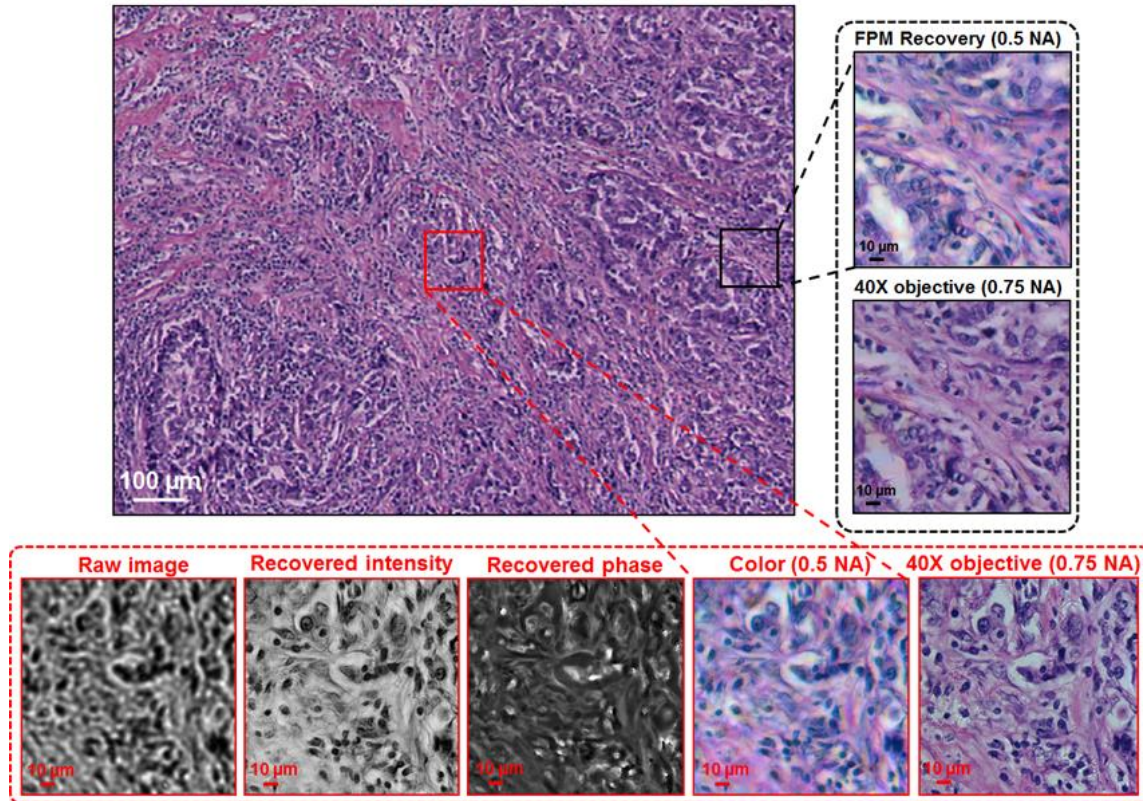


Fig. 5.6 Demonstration of the FPscope using a pathology slide. The full field-of-view is about 1.2 mm by 0.9 mm. The maximum synthetic NA is 0.5. Images captured using conventional microscope with a 0.75 NA objective lens are also shown for comparison.

## Chapter 6

### Conclusion

In chapter 2, In conclusion, we have investigated the data redundancy requirements of the FP approach in both the spectral and spatial domains. We have reported a sparsely sampled FP scheme by selectively updating the pixel values in the spatial domain. Such a scheme is able to get rid of the multi-exposure acquisition process in the original FP platform, and considerably shortens the acquisition time. We have also discussed a sub-sampled FP scheme and used it solve the pixel aliasing problem plagued in the original FP setting. Our on-going effort includes the development of single-pixel FP by using the sub-sampled scheme. Finally, we note that, the data redundancy requirements may also depend on the chosen samples. The relationship between the image compressibility and the data redundancy requirement deserves further investigations. This relationship can also be related to the recent development of compressive sensing [21]. The study in this paper, however, provides an engineering guideline on designing FP experiments.

In chapter 3, we have developed and demonstrated an imaging technique, termed pattern-illuminated Fourier ptychography, for high-resolution fluorescence imaging. This approach recovers a high-resolution sample image from many pattern-illuminated low-resolution images. We reiterate that, the use of non-uniform intensity patterns for sample illumination is not a new idea. It has been demonstrated in various imaging settings for improving lateral/axial resolution [36–44]. However, the use of the FP framework for recovering the high-resolution fluorescence image is new and may provide an alternative solution for the existing SIM and speckle illuminating settings. There are several advantages associated with the reported approach. 1) It is compatible to most existing fluorescence microscope platforms; no major hardware modification is needed. The experimental demonstration presented in this work was performed at a commercially available

microscope platform. 2) The rich literatures on correction schemes of FP and conventional ptychography can be integrated into the reported framework. For example, the pupil correction scheme and the related adaptive system correction scheme in FP can be integrated into the reported framework for factoring out system uncertainties. The positional correction scheme used in the conventional ptychography approach can also be integrated into the reported framework to correct for positional uncertainty. 3) The reported approach is very efficient in terms of computational cost. The solution typically converges with 5-15 loops. In our experimental demonstration, we used 5-9 loops for recovering the images shown in Fig. 25(a1)-(d1). The corresponding computational time is less than one second using an Intel i7 CPU. The reported algorithm is also highly parallelizable. As a result, the computational time can be significantly shortened using a GPU. 4) The mechanical scanning range of the reported approach is on the order of speckle size. Therefore, the scanning process is considered very fast compared to the conventional sample scanning process, where the scanning range is on the scale of sample size. In our implementation, we use 1  $\mu\text{m}$  scanning step and the entire scanning region is restricted within 7  $\mu\text{m}$  by 7  $\mu\text{m}$ . There are two limitations associated with the current experimental setting. 1) The epi-illuminated configuration uses the same objective lens for light delivering and light collection. Therefore, it limits the maximum resolution enhancement factor to 2. It would be straight forward to decouple the illumination NA from the collection NA using a transmission configuration. For example, we can use a high-NA condenser lens to produce high-frequency speckle patterns. We can then use a low-NA lens to capture raw images. The final resolution is determined by the high-NA condenser lens while the final field-of-field is determined by the low-NA objective lens. In this regard, it is possible to use the reported approach to develop high-throughput gigapixel fluorescence imaging platform. 2) In the current implementation, the sample scanning positions are assumed to be the

known information. This assumption requires the use of precise mechanical stages. However, we note that, it is possible to recover the scanning positions from the cross-correlation of the acquired images. Therefore, it is possible to recover the high-resolution image without knowing the scanning positions of the sample.

In chapter 4, we have developed and demonstrated an imaging technique, termed pattern-illuminated Fourier ptychography, for high-resolution fluorescence imaging. This approach recovers a high-resolution sample image from many pattern-illuminated low-resolution images. We reiterate that, the use of non-uniform intensity patterns for sample illumination is not a new idea. It has been demonstrated in various imaging settings for improving lateral or axial resolution. However, the use of the FP framework for recovering a high-resolution fluorescence image is new and may provide an alternative solution for the existing SIM and speckle illuminating platforms. There are several advantages associated with the reported approach. 1) It is compatible with most existing fluorescence microscope platforms; no major hardware modification is needed. The experimental demonstration presented in this work was performed on a commercially available microscope platform. 2) The rich literatures on correction schemes of FP and conventional ptychography can be integrated into the reported framework. For example, the pupil correction scheme and the adaptive system correction scheme in FP can be integrated into the reported framework for factoring out system uncertainties. The sparsely sampled FP scheme can be used in the reported framework to bypass the pixel aliasing problem. 3) The reported approach is very efficient in terms of computational cost. The solution typically converges with 5-20 loops. In our experimental demonstration, we used 5-15 loops for recovering the images shown in Fig. 12(a1)-(d1). The corresponding computational time is less than one second using an Intel i7 CPU. The reported algorithm is also highly parallelizable. As a result, the computational time can be

significantly shortened using a graphical processing unit (GPU). 4) The mechanical scanning range of the reported approach is on the order of speckle size. Therefore, the scanning process is considered very fast compared to the conventional sample scanning process, where the scanning range is on the scale of sample size. In our implementation, the entire scanning region is restricted within  $15\ \mu\text{m}$  by  $15\ \mu\text{m}$ . There are three limitations associated with the current experimental setting. 1) The epi-illumination configuration uses the same objective lens for light delivering and light collection. Therefore, it limits the maximum resolution enhancement factor to 2. It would be straight forward to decouple the illumination NA from the collection NA using a transmission configuration. For example, we can use a high-NA condenser lens to produce high-frequency speckle patterns. We can then use a low-NA lens to capture raw images. The final resolution is determined by the high-NA condenser lens while the final field-of-view is determined by the low-NA objective lens. In this regard, it is possible to use the reported approach to develop a high-throughput gigapixel fluorescence imaging platform. Such a development will be complementary to the gigapixel bright-field microscopy using the original FP approach. 2) In the current implementation, the sample scanning positions are assumed to be the known information. This assumption requires the use of precise mechanical stages. However, we note that, it is possible to recover the scanning positions from the cross-correlation of the acquired images. Therefore, it is possible to recover the high-resolution image without knowing the scanning positions of the sample. 3) We assume the sample is a 2D section in the reported framework. Modelling the reported FP framework using 3D optical transfer function and 3D speckle patterns is one of our future directions.

In chapter 5, we have reported a compact, lightweight, low-cost, and high-resolution microscope platform that we termed FPscope. There are several advantages of the reported

platform: 1) the resolution of the reported platform is determined by the largest incident angle of the illumination, not the NA of the cellphone lens and, therefore, we are able to eliminate the traditional reliance on a high-NA lens. 2) Aberrations of the cellphone lens are compensated by the complex pupil function introduced to the FPscope. We have demonstrated the use of a second order defocused pupil function to extend the depth-of-focus beyond the physical limit of the lens. 3) The rich literature on FP can be integrated into the reported framework. For example, the pupil correction scheme [71] and the adaptive system correction scheme [70] in FP can be integrated into the reported framework for factoring out system uncertainties, such the position of the sample, the intensity of the LED array, the position of the LED array and etc. The sparsely sampled FP scheme [27] can be used in the reported framework to bypass the pixel aliasing problem. The multispectral scheme can also be used in the FPscope to perform information multiplexing [58]. Finally, we reiterate that the use of a lens in the reverse manner is not a new idea. It has been demonstrated in our previous work on gigapixel imaging [73]. However, the use of a reversed cellphone lens in conjunction with the FP algorithm enables a cost-effective solution for field-portable microscopy imaging, which may allow healthcare access in resource-limited environments.

## Reference

- [1] M. Guizar-Sicairos and J. R. Fienup, BPhase retrieval with transverse translation diversity: A nonlinear optimization approach, *Opt. Exp.*, vol. 16, no. 10, pp. 7264–7278, May 2008.
- [2] G. Zheng, R. Horstmeyer, and C. Yang, Wide-field, high-resolution Fourier ptychographic microscopy, *Nat. Photon.*, vol. 7, no. 9, pp. 739–745, Sep. 2013.
- [3] X. Ou, R. Horstmeyer, C. Yang, and G. Zheng, Quantitative phase imaging via Fourier ptychographic microscopy, *Opt. Lett.*, vol. 38, no. 22, pp. 4845–4848, Nov. 2013.
- [4] W. Hoppe and G. Strube, Diffraction in inhomogeneous primary wave fields. 2. Optical experiments for phase determination of lattice interferences, *Acta Crystallogr. A, Found. Crystallogr.*, vol. 25, pp. 502–507, 1969.
- [5] H. M. L. Faulkner and J. M. Rodenburg, Movable aperture lensless transmission microscopy: A novel phase retrieval algorithm, *Phys. Rev. Lett.*, vol. 93, no. 2, pp. 023903-1–023903-4, Jul. 2004.
- [6] P. Thibault, M. Dierolf, A. Menzel, O. Bunk, C. David, and F. Pfeiffer, High-resolution scanning X-ray diffraction microscopy, *Science*, vol. 321, no. 5887, pp. 379–382, Jul. 2008.
- [7] P. Thibault, M. Dierolf, O. Bunk, A. Menzel, and F. Pfeiffer, Probe retrieval in ptychographic coherent diffractive imaging, *Ultramicroscopy*, vol. 109, no. 4, pp. 338–343, Mar. 2009.
- [8] M. Dierolf, P. Thibault, A. Menzel, C. M. Kewish, K. Jefimovs, I. Schlichting, K. von Koenig, O. Bunk, and F. Pfeiffer, Ptychographic coherent diffractive imaging of weakly scattering specimens, *New J. Phys.*, vol. 12, no. 3, p. 035017, Mar. 2010.
- [9] A. M. Maiden, J. M. Rodenburg, and M. J. Humphry, Optical ptychography: A practical implementation with useful resolution, *Opt. Lett.*, vol. 35, no. 15, pp. 2585–2587, Aug. 2010.
- [10] Hüe, F., et al. "Extended ptychography in the transmission electron microscope: Possibilities and limitations." *Ultramicroscopy* 111.8 (2011): 1117-1123.
- [11] Shenfield, Alex, and John M. Rodenburg. "Evolutionary determination of experimental parameters for ptychographical imaging." *Journal of Applied Physics* 109.12 (2011): 124510.
- [12] Humphry, M. J., et al. "Ptychographic electron microscopy using high-angle dark-field scattering for sub-nanometre resolution imaging." *Nature communications* 3 (2012): 730.
- [13] Edo, T. B., et al. "Sampling in x-ray ptychography." *Physical Review A* 87.5 (2013): 053850.
- [14] Marchesini, Stefano, et al. "Augmented projections for ptychographic imaging." *Inverse Problems* 29.11 (2013): 115009.
- [15] Marchesini, Stefano, et al. "Augmented projections for ptychographic imaging." *Inverse Problems* 29.11 (2013): 115009.
- [16] R. Horstmeyer and C. Yang, BA phase space model of Fourier ptychographic microscopy, *Opt. Exp.*, vol. 22, no. 1, pp. 338–358, Jan. 2014.
- [17] M. J. Booth, Adaptive optics in microscopy, *Philos. Trans. Roy. Soc. London A, Math. Phys. Sci.*, vol. 365, no. 1861, pp. 2829–2843, Dec. 2007.
- [18] D. Debarre, M. J. Booth, and T. Wilson, Image based adaptive optics through optimisation of low spatial frequencies, *Opt. Exp.*, vol. 15, no. 13, pp. 8176–8190, Jun. 2007.
- [19] J. Fienup and J. Miller, Aberration correction by maximizing generalized sharpness metrics, *J. Opt. Soc. Amer. A, Opt. Image Sci.*, vol. 20, no. 4, pp. 609–620, Apr. 2003.
- [20] Z. Bian, S. Dong, and G. Zheng, Adaptive system correction for robust Fourier ptychographic imaging, *Opt. Exp.*, vol. 21, no. 26, pp. 32 400–32 410, Dec. 2013.
- [21] R. G. Baraniuk, "Compressive sensing [lecture notes]," *IEEE Sig. Proc. Mag.* 24(4), 118–121 (2007).

- [22] E. Wolf, "New theory of partial coherence in the space-frequency domain. Part I: spectra and cross spectra of steady-state sources," *J. Opt. Soc. Am.* 72(3), 343–351 (1982).
- [23] L. W. Whitehead, G. J. Williams, H. M. Quiney, D. J. Vine, R. A. Dilanian, S. Flewett, K. A. Nugent, A. G. Peele, E. Balaur, and I. McNulty, "Diffractive Imaging Using Partially Coherent X Rays," *Phys. Rev. Lett.* 103(24), 243902 (2009).
- [24] B. Abbey, L. W. Whitehead, H. M. Quiney, D. J. Vine, G. A. Cadenazzi, C. A. Henderson, K. A. Nugent, E. Balaur, C. T. Putkunz, A. G. Peele, G. J. Williams, and I. McNulty, "Lensless imaging using broadband X-ray sources," *Nat. Photonics* 5(7), 420–424 (2011).
- [25] P. Thibault and A. Menzel, "Reconstructing state mixtures from diffraction measurements," *Nature* 494(7435), 68–71 (2013).
- [26] D. J. Batey, D. Claus, and J. M. Rodenburg, "Information multiplexing in ptychography," *Ultramicroscopy* 138, 13–21 (2014).
- [27] S. Dong, Z. Bian, R. Shiradkar, and G. Zheng, "Sparsely sampled Fourier ptychography," *Opt. Express* 22(5), 5455–5464 (2014).
- [28] M. N. Gurcan, L. E. Boucheron, A. Can, A. Madabhushi, N. M. Rajpoot, and B. Yener, "Histopathological image analysis: A review," *IEEE Rev. Biomed. Eng.* 2, 147–171 (2009).
- [29] H. Akbari, L. V. Halig, D. M. Schuster, A. Osunkoya, V. Master, P. T. Nieh, G. Z. Chen, and B. Fei, "Hyperspectral imaging and quantitative analysis for prostate cancer detection," *J. Biomed. Opt.* 17(7), 0760051(2012).
- [30] F. Woolfe, M. Maggioni, G. Davis, F. Warner, R. Coifman, and S. Zucker, "Hyper-spectral microscopic discrimination between normal and cancerous colon biopsies," *IEEE Trans. Med. Imaging* 99, 9999 (1999).
- [31] D. T. Dicker, J. Lerner, P. Van Belle, S. F. Barth, D. Guerry 4th, M. Herlyn, D. E. Elder, and W. S. El-Deiry, "Differentiation of Normal Skin and Melanoma using High Resolution Hyperspectral Imaging," *Cancer Biol. Ther.* 5(8), 1033–1038 (2006).
- [32] K. Hoshino, P. P. Joshi, G. Bhave, K. V. Sokolov, and X. Zhang, "Use of colloidal quantum dots as a digitally switched swept light source for gold nanoparticle based hyperspectral microscopy," *Biomed. Opt. Express* 5(5), 1610–1615 (2014).
- [33] D. Brady and M. Gehm, "Compressive imaging spectrometers using coded apertures," in *Defense and Security Symposium*, (International Society for Optics and Photonics, 2006), 62460A–62460A.
- [34] M. Parmar, S. Linsel, and B. A. Wandell, "Spatio-spectral reconstruction of the multispectral datacube using sparse recovery," in *Image Processing, 2008. ICIP 2008. 15th IEEE International Conference on*, (IEEE, 2008), 473–476.
- [35] R. Willett, M. E. Gehm, and D. J. Brady, "Multiscale reconstruction for computational spectral imaging," in *Electronic Imaging 2007*, (International Society for Optics and Photonics, 2007), 64980L–64980L–64915. 1.
- [36] M. G. Gustafsson, "Surpassing the lateral resolution limit by a factor of two using structured illumination microscopy," *J. Microsc.* 198(2), 82–87 (2000).
- [37] M. G. Gustafsson, "Nonlinear structured-illumination microscopy: wide-field fluorescence imaging with theoretically unlimited resolution," *Proc. Natl. Acad. Sci. U.S.A.* 102(37), 13081–13086 (2005).
- [38] M. G. Gustafsson, L. Shao, P. M. Carlton, C. J. Wang, I. N. Golubovskaya, W. Z. Cande, D. A. Agard, and J. W. Sedat, "Three-dimensional resolution doubling in wide-field fluorescence microscopy by structured illumination," *Biophys. J.* 94(12), 4957–4970 (2008).



- [39] R. Heintzmann and M. G. Gustafsson, "Subdiffraction resolution in continuous samples," *Nat. Photonics* 3(7), 362–364 (2009).
- [40] P. Kner, B. B. Chhun, E. R. Griffis, L. Winoto, and M. G. Gustafsson, "Super-resolution video microscopy of live cells by structured illumination," *Nat. Methods* 6(5), 339–342 (2009).
- [41] E. Mudry, K. Belkebir, J. Girard, J. Savatier, E. Le Moal, C. Nicoletti, M. Allain, and A. Sentenac, "Structured illumination microscopy using unknown speckle patterns," *Nat. Photonics* 6(5), 312–315 (2012).
- [42] A. Jost and R. Heintzmann, "Superresolution multidimensional imaging with structured illumination microscopy," *Annu. Rev. Mater. Res.* 43(1), 261–282 (2013).
- [43] J. Min, J. Jang, D. Keum, S.-W. Ryu, C. Choi, K.-H. Jeong, and J. C. Ye, "Fluorescent microscopy beyond diffraction limits using speckle illumination and joint support recovery," *Sci. Rep.* 3, 2075 (2013).
- [44] P. T. C. So, H.-S. Kwon, and C. Y. Dong, "Resolution enhancement in standing-wave total internal reflection microscopy: a point-spread-function engineering approach," *J. Opt. Soc. Am. A* 18(11), 2833–2845 (2001).
- [45] J. García, Z. Zalevsky, and D. Fixler, "Synthetic aperture superresolution by speckle pattern projection," *Opt. Express* 13(16), 6073–6078 (2005).
- [46] A. Gur, D. Fixler, V. Micó, J. Garcia, and Z. Zalevsky, "Linear optics based nanoscopy," *Opt. Express* 18(21), 22222–22231 (2010).
- [47] C. Ventalon and J. Mertz, "Quasi-confocal fluorescence sectioning with dynamic speckle illumination," *Opt. Lett.* 30(24), 3350–3352 (2005).
- [48] C. Ventalon and J. Mertz, "Dynamic speckle illumination microscopy with translated versus randomized speckle patterns," *Opt. Express* 14(16), 7198–7209 (2006).
- [49] C. Ventalon, R. Heintzmann, and J. Mertz, "Dynamic speckle illumination microscopy with wavelet prefiltering," *Opt. Lett.* 32(11), 1417–1419 (2007).
- [50] Z. R. Hoffman and C. A. DiMarzio, "Structured illumination microscopy using random intensity incoherent reflectance," *J. Biomed. Opt.* 18(6), 061216 (2013).
- [51] M. A. Neil, R. Juskaitis, and T. Wilson, "Method of obtaining optical sectioning by using structured light in a conventional microscope," *Opt. Lett.* 22(24), 1905–1907 (1997).
- [52] J. G. Walker and K. I. Hopcraft, "A diffuser-based optical sectioning fluorescence microscope," *Meas. Sci. Technol.* 24(12), 125404 (2013).
- [53] D. Dan, M. Lei, B. Yao, W. Wang, M. Winterhalder, A. Zumbusch, Y. Qi, L. Xia, S. Yan, and Y. Yang, "DMDbased LED-illumination Super-resolution and optical sectioning microscopy," *Sci. Rep.* 3, 1116 (2013).
- [54] K. Wicker, "Non-iterative determination of pattern phase in structured illumination microscopy using autocorrelations in Fourier space," *Opt. Express* 21(21), 24692–24701 (2013).
- [55] R. Ayuk, H. Giovannini, A. Jost, E. Mudry, J. Girard, T. Mangeat, N. Sandeau, R. Heintzmann, K. Wicker, K. Belkebir, and A. Sentenac, "Structured illumination fluorescence microscopy with distorted excitations using a filtered blind-SIM algorithm," *Opt. Lett.* 38(22), 4723–4726 (2013).
- [56] J. Pawley, *Handbook of Biological Confocal Microscopy* (Springer, 2010).
- [57] A. Williams, J. Chung, X. Ou, G. Zheng, S. Rawal, Z. Ao, R. Datar, C. Yang, and R. Cote, "Fourier ptychographic microscopy for filtration-based circulating tumor cell enumeration and analysis," *J. Biomed. Opt.* 19(6), 066007 (2014).
- [58] S. Dong, R. Shiradkar, P. Nanda, and G. Zheng, "Spectral multiplexing and coherent-state decomposition in Fourier ptychographic imaging," *Biomed. Opt. Express* 5(6), 1757–1767 (2014).

- [59] J. R. Fienup, "Phase retrieval algorithms: a comparison," *Appl. Opt.* 21(15), 2758–2769 (1982).
- [60] R. A. Gonsalves, "Phase retrieval and diversity in adaptive optics," *Opt. Eng.* 21(5), 215829 (1982).
- [61] B. H. Dean and C. W. Bowers, "Diversity selection for phase-diverse phase retrieval," *J. Opt. Soc. Am. A* 20(8), 1490–1504 (2003).
- [62] X. Heng, D. Erickson, L. R. Baugh, Z. Yaqoob, P. W. Sternberg, D. Psaltis, and C. Yang, "Optofluidic microscopy--a method for implementing a high resolution optical microscope on a chip," *Lab Chip* 6(10), 1274–1276 (2006).
- [63] W. Bishara, T.-W. Su, A. F. Coskun, and A. Ozcan, "Lensfree on-chip microscopy over a wide field-of-view using pixel super-resolution," *Opt. Express* 18(11), 11181–11191 (2010).
- [64] G. Zheng, S. A. Lee, S. Yang, and C. Yang, "Sub-pixel resolving optofluidic microscope for on-chip cell imaging," *Lab Chip* 10(22), 3125–3129 (2010).
- [65] G. Zheng, S. A. Lee, Y. Antebi, M. B. Elowitz, and C. Yang, "The ePetri dish, an on-chip cell imaging platform based on subpixel perspective sweeping microscopy (SPSM)," *Proc. Natl. Acad. Sci. U.S.A.* 108(41), 16889–16894 (2011).
- [66] W. Xu, M. H. Jericho, I. A. Meinertzhagen, and H. J. Kreuzer, "Digital in-line holography for biological applications," *Proc. Natl. Acad. Sci. U.S.A.* 98(20), 11301–11305 (2001).
- [67] A. R. Miller, G. L. Davis, Z. M. Oden, M. R. Razavi, A. Fateh, M. Ghazanfari, F. Abdolrahimi, S. Poorazar, F. Sakhaie, R. J. Olsen, A. R. Bahrmand, M. C. Pierce, E. A. Graviss, and R. Richards-Kortum, "Portable, Battery- Operated, Low-Cost, Bright Field and Fluorescence Microscope," *PLoS ONE* 5(8), e11890 (2010).
- [68] D. N. Breslauer, R. N. Maamari, N. A. Switz, W. A. Lam, and D. A. Fletcher, "Mobile Phone Based Clinical Microscopy for Global Health Applications," *PLoS ONE* 4(7), e6320 (2009).
- [69] A. Skandarajah, C. D. Reber, N. A. Switz, and D. A. Fletcher, "Quantitative Imaging with a Mobile Phone Microscope," *PLoS ONE* 9(5), e96906 (2014).
- [70] V. Mico, Z. Zalevsky, P. Garcia-Martinez, and J. Garcia, "Single-step superresolution by interferometric imaging," *Opt. Express* 12(12), 2589–2596 (2004).
- [71] V. Micó, Z. Zalevsky, and J. Garcia, "Superresolved common-path phase-shifting digital inline holographic microscopy using a spatial light modulator," *Opt. Lett.* 37(23), 4988–4990 (2012).
- [72] G. Zheng, X. Ou, and C. Yang, "0.5 gigapixel microscopy using a flatbed scanner," *Biomed. Opt. Express* 5(1), 1–8 (2014).
- [73] T. R. Hillman, T. Gutzler, S. A. Alexandrov, and D. D. Sampson, "High-resolution, wide-field object reconstruction with synthetic aperture Fourier holographic optical microscopy," *Opt. Express* 17(10), 7873–7892(2009).
- [74] J. R. Fienup, "Phase retrieval algorithms: a comparison," *Appl. Opt.* 21(15), 2758–2769 (1982).
- [75] J. Rodenburg, "Ptychography and related diffractive imaging methods," *Adv. Imaging Electron Phys.* 150, 87– 184 (2008).
- [76] Dong, Siyuan, et al. "FPscope: a field-portable high-resolution microscope using a cellphone lens." *Biomedical optics express* 5.10 (2014): 3305-3310.
- [77] Dong, Siyuan, et al. "High-resolution fluorescence imaging via pattern-illuminated Fourier ptychography." *Optics express* 22.17 (2014): 20856-20870.